CENTRO DE INVESTIGACIONES
EN ÓPTICA, A.C.

THESIS

HYDROPHONES BASED ON INTERFEROMETRIC FIBER-OPTIC SENSORS WITH APPLICATIONS IN PHOTOACOUSTICS

Submitted in partial fulfilment of the requirements to obtain the degree of:

Master of Optomechatronics

Presented by:

Amanda Desireé Salas-Caridad, B. Eng.

Advisor:

Geminiano D. Martínez-Ponce, Ph. D.

· August 2017·

León, Guanajuato, Mexico

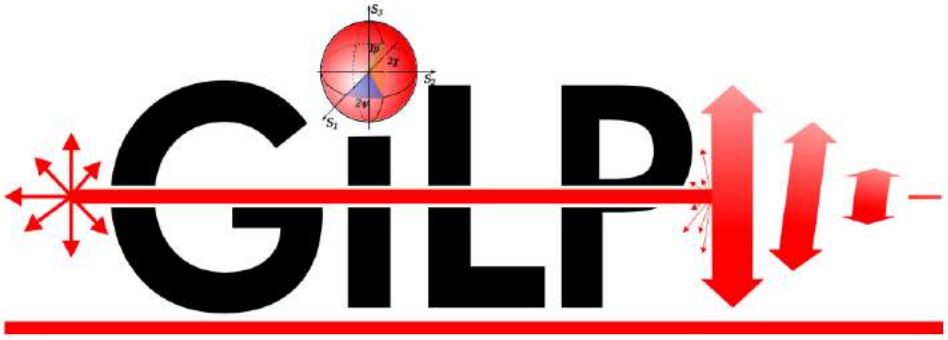

GRUPO DE INVESTIGACIÓN EN LUZ POLARIZADA E IMAGENOLOGÍA

A mi familia:
Milagros, Duglas, Diego y Mary.

Agradecimentos

A mis padres, Milagros y Duglas, por todo el apoyo, la comprensión, y el amor brindados durante esta etapa. A mi hermano, Diego, por tu cariño incondicional y por sentirte siempre orgulloso de mi.

A mi tía, Mary Elizabeth, por tu amor, y por ser pieza importante en todos mis logros y en mi crecimiento emocional.

A mi asesor, papá académico y amigo, el doctor Geminiano, por confiar en mí, acompañarme en este camino y por todas las lecciones de vida que me llevo.

A la mejor amiga, Fabiola, por seguir de cerca mis triunfos y nunca dejarme caer.

A mi amigo, Marthoz, por tus consejos, tu amistad y por hacer más divertido este proceso.

A mis compañeros de maestría, por todo el buen trabajo en equipo, las horas de estudio y las risas.

Al Consejo Nacional de Ciencia y Tecnología (CONACyT) y al Centro de Investigaciones en Óptica (CIO), por todo el apoyo brindado durante mis estudios de maestría.

A mis sinodales, los Dres. Rodolfo Martínez y Gerardo Gutiérrez, por sus valiosos consejos y su tiempo.

A los técnicos del taller mecánico y de los laboratorios de Optomecatrónica del CIO.

A Rosario y Lucy, por su cariño y atenciones en la hora del café.

A todos, ¡muchísimas gracias!

Contents

List of Figures

Abstract

Biomedical imaging used for medical diagnosis constantly requires improvement in the characteristics for imaging devices. The sensing devices are one of the most important pieces to improve in order to get images with better quality. In this thesis, it is proposed the use of interferometric fiber-optic sensors (which offer the advantages inherent to optical fibers) as devices to detect pressure/acoustic signals generated by the photoacoustic effect.

Photoacoustics is a technique which combines the advantages of optics and acoustics. The optics field provides with spectral selectivity, while acoustics provides higher spatial resolution and penetration depth. The applications on this field are currently mainly oriented to biomedics, but many other applications can be tested by following this principle.

In this work, it is explored the capability of using fiber-optic interferometric hydrophones in order to determine the thickness of a material derived from the acoustic signal generated when a sample is illuminated. For this case, rubber and aluminium slabs with different thicknesses were the studied samples.

In addition, the analysis of photoacoustic signals generated by the excitation of nanoparticles of an anisotropic material as absorption centers. The experiments consisted on analyzing the generated signals at different wavelengths, with different polarization states of the excitation beam, and the change in the signal when a tensile strength is applied.

Finally, the cross-section of a metallic sample was photoacoustically imaged by acquiring the pressure signals generated. These signals were processed to form a pressogram. In order to reconstruct the image, a time set of ultrasound signals acquired in a circular scan around the sample were used to solve the time-reversal reconstruction equations. It was observed that image contrast can be enhanced considering the deconvolution of the sensor frequency response from each measured pressure signal.

The results from the experiment, allowed to observe the ability of the hydrophones to be suitable for different photoacoustic applications. The specific goals for this thesis were achieved and throw conclusions on the improvements that can be done and the possible future work with the hydrophones in similar experimental setups, and for different photoacoustic applications.

Chapter 1

Introduction

In this chapter, information on the state of the art is revised. In order to approach the objectives of this work in a accurate way, background information is given on sensing technologies first.

It is intended to detect acoustic waves (ultrasound waves) with frequencies up to tens of megahertz in this work. Because of this, background information will be reviewed on acoustic sensing, particularly, different types and configurations for ultrasound (piezoelectric/ceramic) sensors.

Optical sensors are also used for ultrasound detection. Specifically, fiber-optic interferometric-based sensing is introduced, and a comparison is made between merit figures in order to find the advantages of using either piezoelectric or optical sensors.

On the other hand, ultrasound imaging is explained as one of the most widely known imaging techniques, before introducing photoacoustics as the application/technique of interest for this thesis. The history, background and importance on photoacoustics will be explained before the thesis contents are summarized at the end of this chapter.

1.1 Sensing technologies

Sensing technologies have become essential and enabling for several areas, such as entertainment, security, medical imaging, and transport, among others. The development of these technologies depends on the different applications and desired sensitivity for

such applications. Features like size and fabrication materials have been improving over the years to achieve higher sensitivities and more accurate measurements. Also, remote and distribuited sensing is often needed for specific solutions on high-scale structures or difficult access locations.

Historical facts show that improving materials science and engineering have driven the development of sensor technologies. For instance, the temperature sensitivity of electrical resistance in a variety of materials was noted in the early 1800s and was applied by Wilhelm von Siemens in 1860 to develop a temperature sensor based on a copper resistor. The high resonance stability of single-crystal quartz, along with its piezoelectric properties, have made possible a wide range of high performance, affordable sensors which play an important role in everyday life [4].

More recently, a new era in sensor technology started with the development of large-scale silicon processing. It permits the exploitation of silicon to create new methods for transducing physical properties into electrical signals. The output can be readily processed by a computer. Ongoing developments in materials technology will permit better control of material properties and behaviour, thereby offering possibilities for new sensors with advanced features, such as greater fidelity, lower cost, and increased reliability.

1.2 Ultrasound

Ultrasound represents maybe the most widely known technique under which the inner constitution of non-transparent and/turbid objects can be imaged and examined. The term ultrasound describes the sound with frequencies above the human hearing limit (> 20 kHz).

The localization of objects by means of sound goes back to the principle of operation of the sonar. An impulse signal is emitted by a transmitter, the signal is partially reflected when it encounters an obstacle. The echo signal is detected by the transmitter as well, if it is built with a reverse architecture (receiver). An ultrasound probe often

consists of both, a transmitter, and a receiver.

The distance from the object is determined partly from the round trip time of the signal, in other words, the whole time the signal takes to hit the object and go back to the receiver. The sound velocity of the medium is the remaining parameter needed to calculate the distance. However, the technique has limitations in resolution and localization accuracy. These natural limits come from the signal frequency components, and from the fluctuations in the sound velocity, and some other factors [5].

1.2.1 Generation and detection of ultrasound

One of the effects by which an ultrasound can be generated or detected is through the piezoelectric effect. Technical ultrasound is usually generated by electrical means.

The common generation setup, places a disk or layer of piezoelectric material between two metal electrodes. When the electrical field between the electrodes experience change due to an alternating voltage applied, the disk reacts to the field variations and varies its thickness. Consequently, it leads to sound emission into the environment.

The piezoelectric effect is reversible, so it can be used for detecting the ultrasound signals. For this case, a sound wave varying the thickness in the piezoelectric material, generates an alternating electric field in the electrodes. On this matter, ultrasound microphones have been developed, usually used in liquid media. These are referred as hydrophones and will be further discussed later in this chapter.

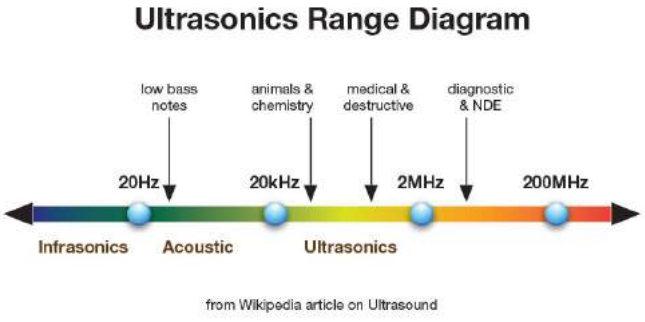

Figure 1.1: Ultrasonics chart diagram

In the following section, some types of ultrasound and acoustic transducers are defined.

1.3 Ultrasound Sensors

1.3.1 Piezoelectric Sensors

1.3.1.1 Microphone

A microphone is an electroacoustical sound receiver which converts acoustical or mechanical vibrations into electrical signals, similar to a piezoelectric transducer. They can be designed either for air-borne or water-borne sound detection. The performance of a microphone depends on several features. Sensitivity is one of them, defined for microphones as the ratio of the open-circuit voltage to the applied sound pressure. Also, the frequency dependence to the sensitivity can be associated to linear distortions. Finally, the directivity of the microphone is another important feature, and it will be defined next.

1.3.1.1.1 Directivity The angle-dependent sensitivity is desired in a microphone when responding to sound pressure. The sound pressure itself does not contain information on the directional structure of a sound field.This implies that the microphone dimensions will be much smaller than the wavelength (easily fulfilled for low frequencies). Most pressure microphones tend to be more directional when exposed to higher frequencies, and their sensitivity depends somehow on the direction of sound incidence.

1.3.1.2 Piezoelectric microphone

A piezoelectric microphone is formed by a diaphragm which is in mechanical contact with a piezoelectric material which transduces any deflection into an electrical signal. Due to the piezoelectric transducer principle, the piezoelectric element has to be deformed by the sound pressure. For a membrane microphone, when the piezoelectric

material is bent, electrical surface charges are produced due to a transversal piezoelectric effect. This effect means that opposite sign electrical charges are produced when the electrodes (plates) are connected in electrical opposition.

For anisotropic piezoelectric material, physical constants can be related to both, the direction of the applied mechanical or electric force and the directions perpendicular to the applied force. Consequently, each constant generally has two subscripts that indicate the directions of the two related quantities, such as stress (force on the ceramic element / surface area of the element) and strain (change in length of element / original length of element) for elasticity [1]. The direction of positive polarization usually is made to coincide with the Z-axis of a rectangular system of X, Y, and Z axes. Positive polarization corresponds to the positive Z-axis values (Fig. 1.2).

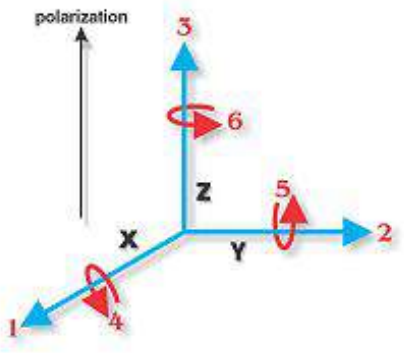

Figure 1.2: Polarization axes and directions for anisotropic piezoelectric materials [1]

Direction X, Y, or Z is represented by the subscript 1, 2, or 3, respectively, and shear about one of these axes is represented by the subscript 4, 5, or 6, respectively. Definitions of the most frequently used constants, and equations for determining and interrelating these constants, are the piezoelectric charge constant, d, the piezoelectric voltage constant, g, and the permittivity, e. These three are temperature dependent factors.

The *piezoelectric charge constant*, d, is the polarization generated per unit of mechanical stress (T) applied to a piezoelectric material or, alternatively, is the mechanical strain (S) experienced by a piezoelectric material per unit of electric field applied. The

first subscript to d indicates the direction of polarization generated in the material when the electric field, E, is zero or, alternatively, is the direction of the applied field strength. The second subscript is the direction of the applied stress or the induced strain, respectively. The piezoelectric charge constant for positive polarization will be d_{33}, the induced strain in direction 3 per unit electric field applied in direction 3.

The piezoelectric voltage constant, g, is the electric field generated by a piezoelectric material per unit of mechanical stress applied or, alternatively, is the mechanical strain experienced by a piezoelectric material per unit of electric displacement applied. The first subscript to g indicates the direction of the electric field generated in the material, or the direction of the applied electric displacement. The second subscript is the direction of the applied stress or the induced strain, respectively. The piezoelectric voltage constant for positive polarization will be g_{33},the induced strain in direction 3 per unit electric displacement applied in direction 3.

The permittivity, or dielectric constant, ϵ, for a piezoelectric ceramic material is the dielectric displacement per unit electric field. ϵ^T is the permittivity at constant stress, ϵ^S is the permittivity at constant strain. The first subscript to ϵ indicates the direction of the dielectric displacement; the second is the direction of the electric field.

For a merit figure comparison, some common piezoelectric materials for detection of acoustic waves, and their respective piezoelectric constants, are presented on Table 1.1

Table 1.1: Piezoelectric materials

Material	g_{33} $[10^{-12}m/V]$	d_{33} $[10^{-13}mV/N]$	ϵ^T_{33} [F/m]
Quartz	N/A	2.3	4.5
Barium Titanate	14.1	149	1200
PVDF	339	33	12
PZT	38.1	152	450

1.3.1.3 Hydrophones

Hydrophones are also known as underwater (or other liquid media) microphones. Most hydrophones are based also on the piezoelectric effect, and they are designed and built in such a way the sound waves interact directly with the transducer material. A hydrophone must be very small in dimensions, compared to the sound wavelength, as for the previous microphone cases.

High-frequency bandwidth sound waves, as the ones detected in this work, are particularly detected by needle hydrophones. These are commonly built as a metal needle with its tip covered with a thin film of a piezoelectric material. Polyvinyldene fluoride (PVDF) is often the material which covers the tip, and it has to be polarized before use.

In order to achieve a needle shape for different hydrophones, and exploit the advantages of other piezoelectric materials, fiber-optic sensors are defined in the following section. These devices can be used to detect high-frequency sound pressure waves. This way, a hydrophone can be built, and take advantage of the characteristics of an optical fiber.

1.3.2 Optical Sensors for Ultrasound Detection

Over the past few decades, there was an increase in the research and development of optical sensors. In particular, fiber-optic based sensors, have been developed into the ability to measure physical parameters such as, temperature, pressure, strain, etc. Fiber-optic sensors have been used to detect acoustic waves in several applications. Integrity monitoring, large civil structure status and hydrophone networks are some of them.

In Table 1.2, some characteristics on materials used for fiber-optic sensors manufacturing, are displayed. Features as the density, refractive index and Young Modulus are parameters which define the elasto-optic effect that occurs when the materials experience perturbation of some kind.

1.3.2.1 Fiber-optic sensors

These sensors exhibit the advantages inherent to optical fibers. Its dielectric nature, low weight and its ability to be under extreme environmental conditions, are some of the attractive features to look at.

The operation principle of an optical fiber sensor is based on changes in the characteristics of the light traveling inside the core of an optical fiber, when a perturbation is applied. These perturbations affect the light parameters; either its intensity, its wavelength, its polarization state, or its optical phase. The ability to measure either of these changes, make the fiber become a sensing device that can be redesigned to measure different physical or chemical parameters [6].

Interferometric techniques are often applied to these sensors to achieve a higher sensitivity.

Sagnac, Michelson or Fabry-Pérot interferometers are often used to detect acoustic waves. Particularly, the Fabry-Pérot interferometer alllows to build cavities inside the fiber. The cavities are sensible to pressure waves which modify their optical path, and which translates into phase changes in the interference signal.

The sensors can be built into a distribuited sensing network. When interferometric sensors are multiplexed, the design often gets more complicated. Fiber Bragg grattings can be multiplexed in wavelength (Wavelength Division Multiplexing, WDM) on the optical fiber [6].

Table 1.2: Elasto-optic materials

Material	Density [g/cm^3]	n	Young Modulus
Fused-silica	6.82	0.566	15.2
Barium nitrate	6.82	0.566	15.2
ZnO	5.5	0.564	33.5
PDMS	1.78	0.22	2.5
Silicone	4.64	0.773	34.0
Parylene-C	7.5	0.460	34.5

1.4 Ultrasound imaging

Ultrasound imaging is a widely used technique, which uses high frequency sound energy to conduct examinations and make measurements. Ultrasonic inspection can be used for flaw detection/evaluation, dimensional measurements, material characterization, and more. A typical ultrasonic inspection system consists of functional units, such as the pulser/receiver, transducer, and display devices. A pulser/receiver is an electronic device that produces high voltage electrical pulses. Driven by the pulser, the transducer generates high frequency ultrasonic (sound) energy which is introduced and propagates through materials in the form of longitudinal waves. When there is a discontinuity in the wave path, part of the energy will be reflected back from the flaw surface. The reflected wave signal is transformed into an electrical signal by the transducer and is displayed on a screen. Signal travel time can be directly related to the distance that the signal traveled. From the echo signal recovered, one can obtain information about the reflector location, size, orientation and other features [7]. Despite the efectivity of the ultrasound techniques, their performance also show limitations in terms of roughness of materials, resolution, signal-to-noise ratio, directivity of the devices, etc.

1.4.1 Ultrasound for diagnostic and medical imaging

Ultrasound techniques play an important role for applications of low-intensity signal detection. Among them, there is the non-destructive testing applications and medical sonography. The latter is probably on of the most widely known imaging tools. In medical sonography, the scanning setup can be either an "A-scan" or a "B-scan". The "C-scan" is a three dimensional scan which repeats the "B-scan" over a sample depth or longitude.

The "A-scan" consists in finding edges of a perturbation to form a medical diagnosis and localization of strange bodies. It is also rarely used as the examining doctor prefers a more detailed image.

The "B-scan" consists of a scan where the sound rays are carried electronically, and

piezoelectric transducer arrays are used for detection.

The high frequency ultrasonic C-scan is a non-destructive technique to examine defects inside a material. This apparatus permits researchers to identify the depth of the observed defect in the sample. This capability makes it a valuable tool to monitor the precise location of delaminations between certain plies, caused by impact or fatigue loading.

A very high frequency signal (up to 50 MHz) is transmitted to the sample by a (focused) transducer. The sample and the transducer are submerged in water that serves as the coupling medium. The initial signal is partially reflected back to the transducer at interfaces, defects, porosities and at strong differences in acoustic impedance in the sample and the rest of the signal, if not fully reflected continues through the sample. On Fig. 1.5, an example of the three types of scan are depicted for one sample.

Ultrasound imaging is useful for examining soft tissues with little impedance difference between its components. The ultrasound beam has a high penetration depth, often able to travel through organs' boundaries. Imaging tissues conveys the visualization of irregular patterns in the structure, caused by the interference of weaker echo components produced by parts of the tissue. Nevertheless, these components provide

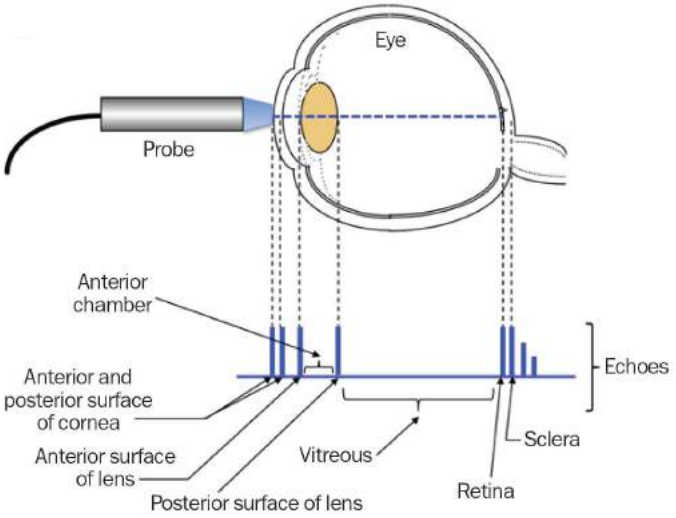

Figure 1.3: A-scan ultrasonics for eye imaging

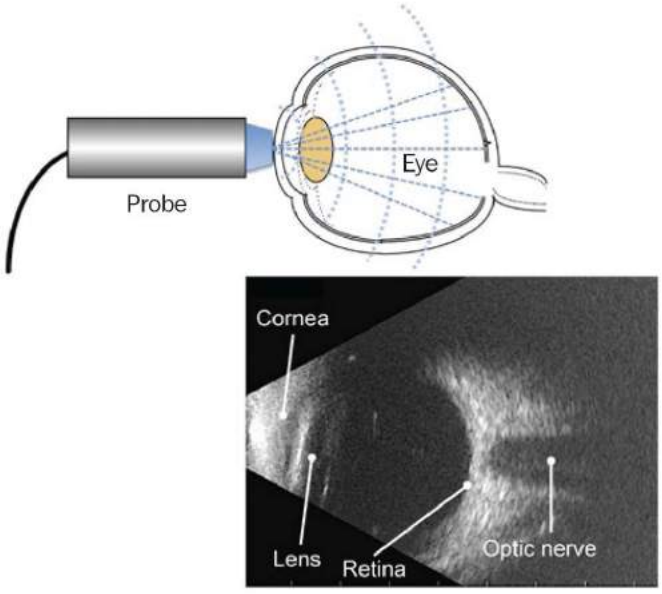

Figure 1.4: B-scan ultrasonics for eye imaging

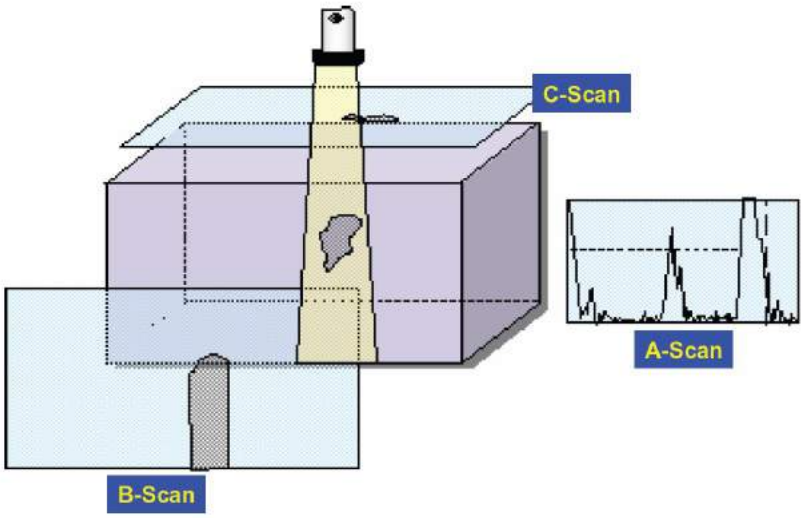

Figure 1.5: Diagram of A-scan, B-scan and C-scan of a sample [**?**].

information on the boundaries between tissues and organs, their location and size.

The surface on some organs or bones cause the sound to be reflected completely, which is why sonography is not suitable for examining these regions. Particularly, sonography presents an advantage over X-rays as it employs non-ionizing radiation, avoiding health risks. The sound energy used for sonography can be so low as to not

affect the tissue due to mechanical strain or overheat.

In the following section, some types of ultrasound and acoustic transducers are defined.

1.5 Photoacoustic effect

Photoacoustics is a hybrid technique driven by the photoacoustic effect. This effect is based on the sensitive detection of acoustic waves launched by the absorption of pulsed or time modulated radiation by an optical center. In this transduction process, electromagnetic energy is changed to mechanical energy by transient localized heating and expansion in a surrounding gas, liquid, or solid. This effect is due to the transformation of at least part of the electromagnetic excitation energy into kinetic (translational) energy in the excited object. Consequently, the absorption of modulated radiation generates an acoustic signal that is monitored by an ultrasonic transducer [8, 9].

It is an interesting hybrid technique which combines the advantages of optics and acoustics. The optics field provides with spectral selectivity, while acoustics provides higher spatial resolution and penetration depth. The technique caught the special attention of biomedical researchers, as the optical absorption of some tissue components such as hemoglobin, oxy-hemoglobin, melanin, bilirubin, lipids and water, allows them to process information regarding their presence [2]. This technique makes use of non-ionizing radiation that is incident on the turbid medium of the sample. It may diminish or avoid the side effects brought by the commonly used ionizing radiation techniques for medical imaging and treatments. Some of the most commonly used imaging techniques such as radiography and tomography, use ionizing radiation: X-rays and gamma rays. Although their short wavelength make possible the penetration into deeper matter and better visualization, the shorter the wavelength, the higher the frequency of the radiation, which also implies higher energy applied. High-energy radiation can break chemical bonds, and in human tissue, this may result in altered structure (and/or function) of cells [10].

Given the evolution of imaging techniques and devices, higher resolution is being required, as well as, less-invasive or non-invasive techniques. This is how photoacoustics started to be considered as a reliable medical imaging technique. So far, one of the most important research lines in Photoacoustic imaging, is breast cancer. Developers and researchers from Kyoto University along with Canon®in Japan, managed to build a prototype of a Photoacoustic Mammogram in 2015, aimed to avoid painful and invasive procedures for diagnostics or monitoring of the disease. On the other hand, it does not mean this prototype is an ultimate version. The fact that the sensors used to recover acoustic signals are piezoelectric, makes the system still vulnerable to noise or electromagnetic interference.

This work aims to propose the design of a fiber-optic interferometric sensor array which localizes the origin of an acoustic signal generated by an infrared light absorption center inside the volume of a semi-opaque medium. The characterization and evaluation of the performance for ultrasonic transducers (hydrophones) based in fiber-optic interferometric sensors must be made in order to develop an accurate inverse algorithm for the localization of an acoustic signal from its spatial and temporal behavior. Also, an experimental method to determine the optimal distribution of ultrasonic transducers can be developed as well.

1.5.1 Background and early days

Photoacoustics first started as a series of experiments which demonstrated the production and/or reproduction of sound by light. By the time of the invention of the telephone by Alexander Graham Bell in 1876, the photosensitivity of selenium had already been discovered in 1873 [11]. This led Bell to adapt this property to the telephone transmission. Bell himself credited A. C. Brown for demonstrating the reproduction of articulate speech by the action of light upon selenium in circuit with a battery and telephone for the first time [2]. These demonstrations were considered as the starting point towards creating a device to produce sound out of light.

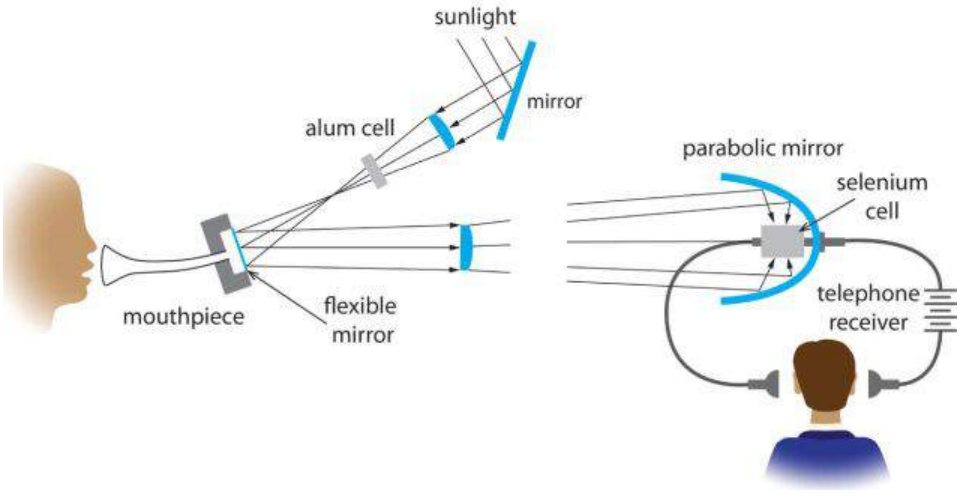

Figure 1.6: Setup of the first Photophone [2].

1.5.1.1 The Photophone

The first well documented evidence of speech transmission by means of light belongs to Bell and his assistant Charles Tainter, who were able to wirelessly transmit voice messages around 213 m in June 1880 [12–15]. Later that year, on August 27, Bell delivered a lecture before the American Association for the Advancement of Science in Boston, in which he presented a functioning apparatus named the *Photophone*.

Figure 1.6 depicts the setup of the first photophone implemented by Bell and Tainter, in which sunlight was focused on the mirror and the associated optics so arranged that the reflected light could be collected by the remotely placed receiver—a parabolic mirror at whose focus a selenium cell incorporated into a conventional telephone circuit was arranged. Speech articulated into the mouthpiece caused the mirror to vibrate, producing fluctuations in the intensity of light collected at the receiver. The voice-modulated intensity of light caught by the receiver as a modulated battery current was converted into sound in the telephone circuit. The selenium-cell photophone can be considered the first practical implementation of wireless telephony or, in fact, the first optical communication device.

The discovery of the Photophone represented a starting point for Bell and several notable scientists to conduct theoretical and experimental research in the matter. After

the publishing of his pioneering paper, "Upon the production and reproduction of sound by light", in April 1881, Bell envisaged a form of communication in which the electrical receiver employed in the selenium-cell variant of the photophone would be replaced by a lamp-black receiver, which would directly convert the light modulations into speech within a range up to a maximum distance of 40m.

From the discovery of this light-induced "sonorous" effect, related theories and explanations of the phenomenon came through the experiments of various scientists. The discoveries are listed below.

- Sounds were obtained from vibrations due to an unequal heating of the diaphragms or plates when illuminated with intermittent light [34,35].
- The cause of the sounds was not the vibration of the absorption media, but rather the expansion and contraction of air in contact with the intermittently heated material.
- The periodic heating and cooling of air in thermal contact with the illuminated sample caused the sound production and this phenomenon was not restricted to solid bodies. One variant of the method could be used to detect extremely small quantities of inflammable gases in mines.

Probably, the most important outcome from this early research was the possibility of eliciting spectral information from samples, from which Bell deduced and concluded that [14] *"the nature of the rays that produce sonorous effects in different substances depends on the nature of the substances that are exposed to the beam, and that the sounds are in every case due to those rays of the spectrum that are absorbed by the body."*

1.5.2 Optoacoustic effect

1.5.2.1 Applications in the 20th century

After the initial excitement, the radiophonic effect lost attention and ended up being part the cited references of 19th century science, principally because experiments were difficult to quantify, as they depended largely on human hearing for signal detection [2].

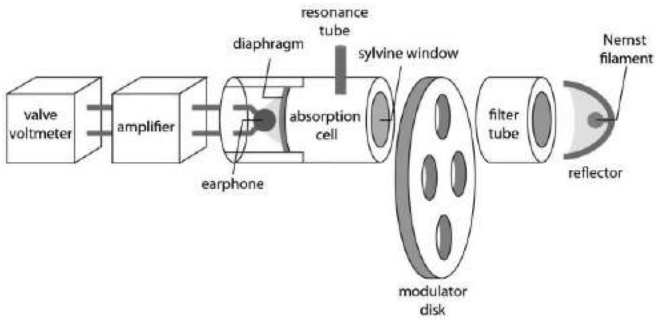

Figure 1.7: Apparatus created by Veingerov for the optico-acoustic analysis of gases [2].

The radiophonic (or photophonic) effect lay dormant for five decades before re-emerging with the work of Mark Veingerov of the State Optical Institute, Leningrad [16], in a technology for infrared gas analysis.

He used state-of-the-art charged capacitive microphone diaphragms and a Nernst glower as an intense blackbody infrared source, to be able to detect CO_2 concentrations in N_2 down to around 0.2 percent of its volume. The setup of the apparatus is shown in Fig. 1.7. Following studies are briefly explained below:

- In 1939, Pfund [17] reported on a similar system in use at the Johns Hopkins Hospital for detection of CO and CO_2 gases. Instead of observing pressure changes, this system directly measured the corresponding changes of gas temperature using a thermopile shielded from direct radiation, avoiding the requirement for acoustic noise isolation.

- Luft introduced a commercial infrared gas analyzer based on microphone detectors, applied in the chemical industry as early as 1938 under the trade name URAS (Ultrarotabsorptionsschreibers—the German for infrared absorption recorder) [18], however, the design was not described in detail until 1943 [19]. It consisted on a double cell (one of them with a contained reference gas, and the other with the species of interest. Two tubes terminated in an adjoining coupled chamber separated by a membrane capacitor as a microphone. Infrared sources interrupted periodically by a rotating disk (chopper) with two sectors generated

the acoustic signals, which were measured as a differential signal from the microphone.

With the development of the laser in 1960, there was yet another revival in gas analysis. As in the case of an excitation cell equipped with an electret microphone. The high powers achievable with laser technology allowed ultralow gas concentration detection and analysis. It was also achievable and desirable to have a high degree of spectral purity, high stability, and reproducibility. Nearly before the 1970s, there were already new reported results in gas analysis using a laser as illumination source.

1.5.3 Pulsed effect

1.5.3.1 Thermal Piston Model

In the physics behind the photophonic effect, a model called "Thermal Piston" can be used to predict the behaviour of a sample to be analyzed inside a chamber. In case it is liquid or solid, it has to be sealed together with a coupling gas [2]. The sample is illuminated with a light beam modulated with a mechanical chopper, the focused intensity is (1.1):

$$I(t) = \frac{I_0}{2}(1 + e^{j\omega t}) \tag{1.1}$$

Where the chopping frequency is $\omega = 2\pi f$. The sample absorbs the incident light and a certain fraction (η) of the energy is converted to heat through non-radiative de-excitation processes. As a result, a periodic heat source is set up in the form of

$$Ae^{\mu_a x}(1 + e^{j\omega t}) \tag{1.2}$$

In (1.2), the amplitude stands as $A = \frac{\mu_a I_0 \eta}{2\kappa}$, where μ_a is the absoption coefficient, x is the depth and κ is the thermal conductivity.

The heat transfer occurs by thermal diffusion, with the rate of transfer controlled by the thermal diffusivity $D = \frac{\kappa}{\rho C}$, where ρ is the mass density and C is the specific heat

capacity. The thermal diffusion phenomena are described by equations with a periodic source term, resulting in time-dependent solutions equivalent to Helmholtz's equations for wave motion. These solutions are the reason why the heat flow is often referred as *thermal wave* [20]. The plane thermal wave T in one dimension has an exponential form

$$T(t, x) = \exp(j\omega t - \sigma x) \tag{1.3}$$

It is dependent on the chopping frequency and a propagation vector σ (Eq. 1.4):

$$\sigma = (1 + j)\sqrt{\frac{\omega}{2D}} \tag{1.4}$$

The heat photothermally deposited in the material is launched as a fast-decaying thermal wave in the sample. In other words, this thermal wave passes through the interface and communicates with the coupling gas, where it decays and only a thin boundary layer of gas experiences temperature changes periodic with the modulation frequency. The periodic expansion and contraction of the gas layer emulates the job of a piston and a train of compressions and rarefactions travel in the rest of the gas in the cell. The sound wave is then recovered by a sensitive microphone placed in the inner wall of the cell. Thermal diffusivity of waves in solids was studied and experimented by Angström in 1861 [21], while the concept photothermally induced sound waves was further studied around the early 1880s by Preece in 1880 [22] and Mercadier in 1881 [23, 24] Also in 1881, Rayleigh [25] and Bell [14] studied the production of an acoustic wave derived from the expansion and contraction of the sample volume. The photothermal induction of sound waves was later developed in the mid-1970s by several other scientists such as Rosencwaig and Gersho [26, 27].

Photothermal spectroscopy is the field in which the nature of matter is probed using optical excitation of the medium and then detecting the thermal energy from this excitation. If this heat is detected appropriately, its measure at varying incident energies can be used to obtain spectral information about the sample. Furthermore, the thermal properties of the sample can also be studied from the heat flow analysis, and

this makes it unique among spectroscopic techniques [20]. In addition to the original gas-microphone approach, there are several other detection techniques (Figure 1.8) based on the measurement of:

1. Pressure changes causing refractive index gradients in an adjacent coupling liquid to periodically deflect a probe laser beam skimming the surface, which is monitored with a position sensitive detector, in photothermal beam deflection spectroscopy [28];

2. Temperature changes using pyroelectric sensors in photopyroelectric spectroscopy [29];

3. Thermal emission changes using infrared detectors, including infrared cameras, in photothermal radiometry [30]; and

4. Vibrations causing acoustic waves in the specimen are picked up with piezoelectric sensors in photoacoustic spectroscopy.

The last mentioned refers to vibrations of the sample due to thermoelastic expansion. This gives us the opportunity to make the link from intensity-modulated to pulsed photoacoustics or optoacoustics.

In the photoacoustics discussed up to this point, the transfer of heat deposited locally takes place via thermal diffusion. The diffusion equation in which the source term has harmonic dependence on time, reduces to a Helmholtz-like equation for wave motion and has wave-like solutions. This is the origin for the use of the term "thermal waves" to describe heat flow in photoacoustic experiments [31].

1.5.3.2 Time-dependent Temperature-Field Solutions

The propagation vector σ contains an imaginary part which is the thermal wave number while the real part leads to rapid attenuation [2].

The wave is damped by a factor e^{-1} at a distance called the thermal diffusion length. Thermal diffusion is thus a highly dissipative process and constitutes heavily damped

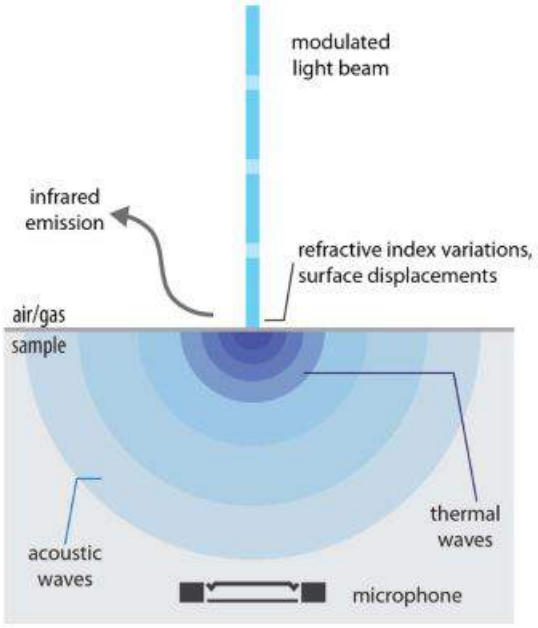

Figure 1.8: A variety of techniques can be applied to probe properties of materials using intermittent light radiation [2].

transport. The second transport mechanism in which there is direct coupling of the heat energy to the vibrational modes of the material. There is a thermoelastic process (thermal expasion involved) in which a pressure build-up is generated, releasing a stress wave. The rate of transfer of this wave is desribed by the speed of sound in the material.

The transfer is generally non-dissipative, except at very high frequencies, where rapid ultrasonic attenuation on a sub-millimeter scale can occur (usually in the hundreds of megahertz range for soft tissues and liquids [32]). The thermoelastic mechanism can be an efficient converter of absorbed energy into acoustic pressure waves, especially if the period of optical excitation is short as shown in figure Fig. 1.9.

If a sample is exposed to a finite-duration heating pulse [33], causing a rapid temperature rise at $x = 0$ from T_0 to T_1, the temperature-field solutions for the heat diffusion equation, when Fourier law is used, will be, for heat flow, as follows:

$$q(x,t) = \frac{T_1 - T_0}{\sqrt{\pi t}} \exp\left(-\frac{x^2}{d_0^2}\right) \tag{1.5}$$

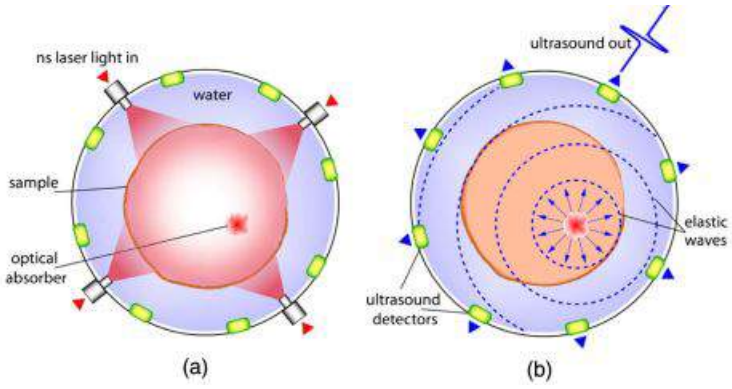

Figure 1.9: Pulsed photoacoustic effect. (a) Scattering sample containing optical absorbers is illuminated with short laser pulses. (b) Absorption of the light energy leads to thermoelastic expansion and subsequent generation of propagating elastic waves that are recorded using detector(s) placed outside the sample [2].

This expression describes a Gaussian spreading of the heat with a *thermal diffusion length* of $d_0 = \sqrt{4Dt_p}$, where t_p is the pulse duration and D is thermal diffusivity of the sample, it is kwown as the thermal confinenement condition. Given this, a pulse of light deposits heat in the optical absorption zone following an exponential decay of light intensity [2]. If the thermal diffusion length happens to be smaller than the resolution of the sensing system, then the heating pulse is so short that thermal diffusion is not significant during the pulse and this would result in no leakage of energy out of the effective optical absorption zone, and maximal thermal energy densities can be attained. This is the thermal confinement regime of pulsed laser heating. If we consider the value of thermal diffusivity to be $D = 0.14\text{mm}^2\text{s}$ in soft biological tissues, this condition can be readily met for typical biological imaging applications that use nanosecond-duration laser pulses [34].

Similarly, a *stress confinement regime* can be defined in which the laser pulse duration is smaller than the time required for the stress propagation out of the heated region defined by the effective spatial resolution [35, 36]. Using pulse durations that satisfy both confinement regimes ensures that the fractional volume expansion $\Delta V/V$ is negligible, i.e. [37]:

$$\frac{\Delta V}{V} = -K\Delta p + \beta\Delta T = 0 \tag{1.6}$$

Where K is the isothermal compressibility, β the coefficient of thermal expansion, Δp the pressure change, and ΔT the temperature change. The initial pressure rise following light absorption can be written as:

$$\Delta p_0 = \frac{\beta \Delta T}{K} = \frac{\beta}{K} \left\{ \frac{E_a}{\rho C_v} \right\} = \frac{\beta}{K} \Delta T \tag{1.7}$$

With ρ the mass density, C_v the specific heat capacity at constant volume, E_a the absorbed optical energy given by the product of μ_a absorption coefficient, and I the fluence at the local absorption point. This can be written as in Eq. 1.8 where Γ is the Grüneisen coefficient and stands as Eq. 1.9. This is a parameter that lumps together the thermal expansion coefficient, the compressibility, and the speed of sound.

$$\Delta p_0 = \Gamma E_a \tag{1.8}$$

$$\Gamma = \frac{\beta}{K \rho C_v} = \frac{\beta v_s^2}{C_p} \tag{1.9}$$

The short excitation pulses thus satisfy both confinement regimes, ensuring that the conversion of temperature rise to a pressure buildup via the Grüneisen coefficient is maximized.

In general, transient heating can be induced by absorption of electromagnetic radiation in various spectra, from radio frequencies and microwaves to ultraviolet, x rays, and electron beams.

Michaels studied for the first time radiant energy transfer at higher heating rates. For experiments, an underwater exploding wire spark was used to produce a light pulse (50μs), which was focused at one end of an aluminum rod. A piezoelectric crystal was mounted at the other end and picked up strong acoustic waves.

1.5.4 Intensity-modulated Photophonic Effect

1.5.4.1 Experiments in solids as the Photoacoustic effect

Interestingly, in gas optoacoustic studies, the accuracy of measurements was known to be limited by the background signal due to absorption and sound production at the walls (and windows) of the cell [16].

The strong resurgence in Bell's effect in solids and liquids was mainly due to researchers at Bell Laboratories, who initiated intensive investigations of the optoacoustic effect in solids in the early 1970s, inspired by the superior sensitivity of the technique in gases previously reported by their colleague Kreuzer. Two articles appeared with work on solids in 1973, one from Rosencwaig [38] and a second from Harshbarger and Robin [39]. The two works used similar instrumentation with a high-pressure Xe lamp and 1/4 monochromator with a chopper, and with electret foil microphones for detection.

While Harshberger and Robin retained Kreuzer's term "optoacoustic" in their paper, Rosencwaig introduced a new term, "photoacoustic", for the effect in solids in order to "avoid any confusion that may result between the original optoacoustic and acousto-optic"; the acousto-optic effect describing the diffraction of light by acoustic waves in a crystal.

Rosencwaig proved through several experiments the exciting possibilities of the technique and the numerous promising applications [40], including for spectroscopy of biological materials such as cytochrome and hemoglobin (Fig. 1.10) [38]. This was soon followed by papers [26, 27] on the theoretical understanding of the effect in solids.

The first imaging studies were conducted on inorganic media such as semiconductors for nondestructive evaluation (NDE) of surface flaws and subsurface inhomogeneities (Fig. 1.11). Signal generation in low-frequency intensity modulated photoacoustics involves the following:

1. Optical absorption

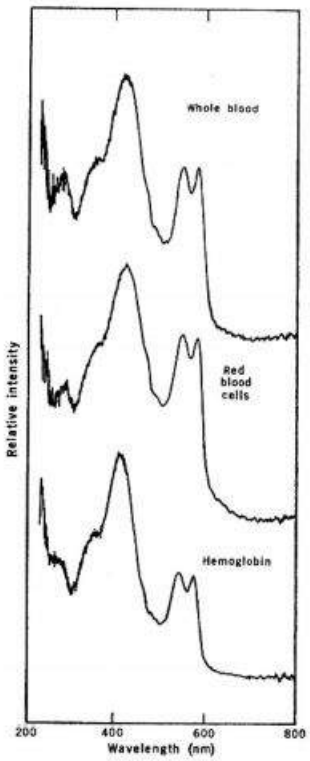

Figure 1.10: Photoacoustic spectra of whole blood, red blood cells, and hemoglobin measured using a Xe lamp and the gas-microphone method [2].

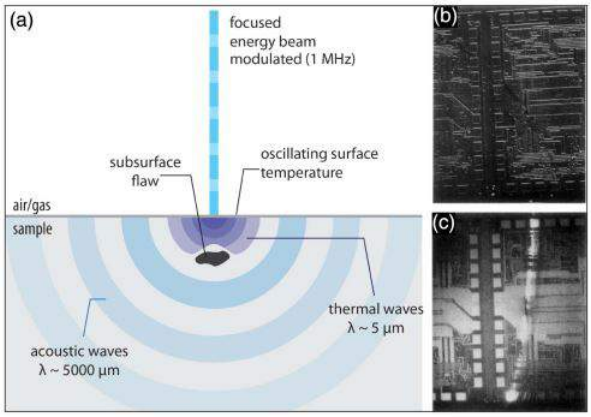

Figure 1.11: (a) Schematic representation of the physical processes that occur during thermal wave imaging. (b) Example of subsurface mechanical defect in silicon integrated circuit that is not visible in backscattered-electron images; (c) thermal-wave microscopy image of the same area reveals a subsurface microcrack. [2].

2. Generation and propagation of thermal waves

3. Generation and propagation of elastic waves.

Thus all three processes can contribute to visualization of the sample. The presence of flaws or inhomogeneities in the illuminated region affects the optical absorption coefficient. Further, the presence of cracks or voids disturbs thermal diffusion wave propagation to give rise to detectable changes in signals.

When elastic waves dominate, the spatial resolution of the image is in a similar range as for conventional ultrasound imaging, which is not the case when optical absorption and thermal waves dominate. The latter occurs in low-frequency modulated photoacoustics, where thermal diffusion plays an important role in signal generation. The resolution in such cases is the wavelength of the thermal waves or the thermal diffusion length, namely, $\sqrt{D/\pi/f}$ (D being the thermal diffusivity and f being the frequency in Hz). However, as mentioned earlier, thermal diffusion is a highly dissipative process and constitutes heavily damped transport, with the wave damped by a factor e^{-1} within the absorption coefficient.

The imaging or penetration depth of the thermal waves is thus a few times the resolution dimensions. Thus, at modulation frequency of $f = 100Hz$ in biological tissue,

the imaging depth is approximately 100μm, which decreases to 1μm when $f = 1$MHz. This constitutes imaging with high resolution, but with low penetration depths, confining applications to the realm of microscopy. Table 1 summarizes the major differences between continuous wave and pulsed photoacoustics.

Table 1.3: Difference between Continuous Wave and Pulsed Photoacoustics [2]

Technique	CW Modulated PA	Short-Pulsed PA
Name of effect	Mostly photothermal. Flow of thermal waves setting up acoustic waves in coupling media	Thermoelasic expansion producing acoustic waves, with minimal heat flow effects
Excitation concept	Low frequency chopping below 1kHz, high duty cycle	Short pulses ($\leq 1\mu$s) in thermal confinement and often in stress confinement; low pulse rep. rates
Generation efficiency	Low	High.
Depth of interrogation for depth-profiling or imaging application	Dependent on the wavelength of the thermal wave, and thus on chopping frequency, but generally low penetration of the order of 100 μm	Depends on the optical excitation wavelength and on the available bandwidth of the ultrasound detector and is usually in the millimiter to centimeter range
Main applications	Spectroscopy of solids, liquids, and gases where samples are too scattering, too absorbing, or too transparent for optical methods. Monitoring of de-excitation channels. Flaw detection and microscopy in non-surface situations	Depth profiling and determination of thin film thickness. Photoacoustic tomography and microscopy of biological tissues. Flow cytometry. Nondestructive testing of solids. Material characterization.

1.5.5 Evolution of Biomedical Applications

The first investigations in the biomedical field of acoustic wave generation by absorption of short light pulses appear to have been conducted in 1964 on the eyes of a living rabbit [3]. The oscillogram from the detector showed a series of acoustic transients corresponding to each of the laser pulses of the normal-mode laser output (Fig. 1.12). The acoustic waves produced by light absorption at the retina propagated through the brain and occipital bone to be detected. These pressure transients were not shock waves, but were elastic wave trains in the ultrasonic regime carrying a main frequency component around 40 KHz.

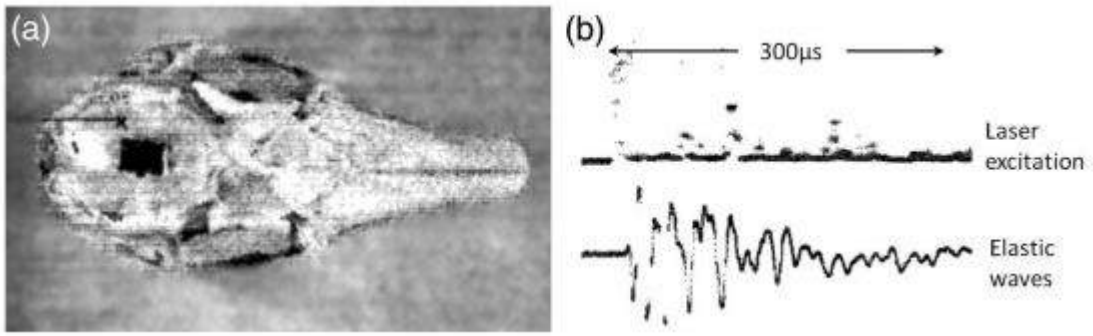

Figure 1.12: First photoacoustic traces acquired from a biological sample. (a) Photograph from the rabbit used in the experiment; (b) opto-acoustic traces obtained from a rabbit retina in vivo using a pulsed ruby laser and barium titanate piezo-electric detector [3].

Other laser-induced ultrasound studies [41] on ex vivo human eye specimens. It helped in the development of a far-fetched theory to explain human vision. It was postulated that when scattered light from an object entered the eye, a lasing action would occur in the retina following absorption by the incoherent photons. This laser emission of coherent photons and their subsequent absorption would induce elastic waves in the retina, which would cause the sensation of sight.

Further studies of laser-induced acoustic transients in the mammalian eye were continued by others [131], mainly for investigating laser-induced damage to the retina. A theoretical analysis in Ref. [42] showed that ultrasound pulses of the same duration as Q-switched laser pulses would be produced.

The observations of auditory responses to pulsed radio-frequency and microwave energies [43–45], spurned interest in the interaction of time-variant electromagnetic energy with tissue in the 1960s and 70's [46]. A theory was put forward by Foster and Finch (1974) [47] in which RF (microwave) energy absorption in tissue caused heating and thermoelastic expansion, resulting in acoustic transients. They showed that pulsed 2.45 GHz radiation produced strong acoustic signals in saline that were detectable with a hydrophone. RF (or microwave) hearing was due to acoustic vibrations in the head of the human, having arrived there after propagation away from the site of heating and via

conduction through bone. Borth and Cain (1977) [48] performed a theoretical analysis of the induced volume and surface forces due to the thermal expansion, electrostriction, and radiation mechanisms in a one-dimensional model. Pressure and displacement waveforms in microwave-irradiated physiological saline as semi-infinite were computed. Thermal expansion was found to be considerably more effective than either electrostriction or radiation pressure in converting electromagnetic energy to acoustic energy.

1.5.5.1 Photoacoustic Imaging in Biological Samples

Photoacoustics thus permitted studies on highly light-scattering materials, such as biological specimens, not amenable to conventional study. Initial studies on biological samples were on investigating the extent of drug incorporation into skin. This was performed by measuring the photoacoustic spectra of skin to find changes in optical absorption due to presence of the drug. Reports on studies of various samples of ex vivo guinea pig epidermis [26] and human stratum corneum [49, 50] treated with medicines such as tetracycline appeared.

Photoacoustic studies on ex vivo human eye lenses were carried out to investigate the processes by which cataracts formed. The spectra from healthy and cataractous lenses showed differences in characteristic absorption peaks of tryptophan and tyrosine residues [49], confirming early theory on the role of these proteins in formation of cataracts.

The thermoelastic mechanism for RF/microwave hearing spurned more research into using radiation in these spectra to generate acoustic signals. Among the first studies to use these acoustic signals for characterizing tissue-like media was from Olsen and Hammer (1980) [51]. They used a radar transmitter to irradiate a muscle phantom with pulsed 5.655 GHz energy, and used a hydrophone to record the acoustic responses. The acoustic waves were found to have pulse durations corresponding to the measured penetration depth of the microwave energy.

Bowen in 1981 [52] was among the first to propose imaging of soft tissues using the method. The paper is titled "Radiation-induced thermoacoustic soft tissue imaging"

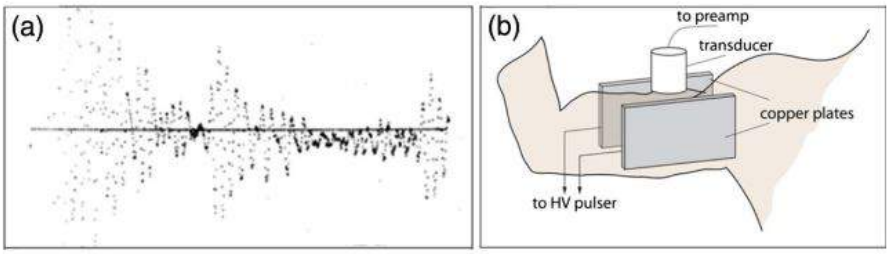

Figure 1.13: (a) Example of a thermoacoustic signal trace recorded from a human arm in vivo. (b) Schematics of the experiment that was used to generate thermoacoustic waves by fast discharge of a high-voltage capacitor. [2]

and describes the phenomenon generally as originating from the deposition of heat into a finite region, using a wide range of radiation, such as RF or microwave energies, high-intensity ultrasound, or ionizing radiation. The paper presents a general solution of the thermoacoustic wave equation in a homogeneous and isotropic medium using the concept of retarded potentials, making an estimate of the signal-to-noise ratios for a point acoustic detector and a focused detector following power-law acoustic attenuation. The article concludes that a practical thermoacoustic imaging system would be possible, and that the method using non-ionizing energies would provide information complementary to conventional imaging methods, such as echography, x-ray imaging, and nuclear isotope imaging. Further, a specific application is mentioned, namely, imaging during therapeutic radiation for dosimetry and treatment planning. In the same year, Bowen et al. [53] showed thermoacoustic A-scans excited using electric currents with copper electrodes inserted in a two-layer phantom comprising muscle-tissue mimicking layered samples topped with vegetable oil. Also in this paper the authors present the first in vivo signals from the upper arm of one of the authors (Fig. 1.13).

1.6 Thesis Contents

This work aims to evaluate the behavior of commercially manufactured fiber-optic interferometric hydrophones for photoacoustic applications.

In the following chapters, the work is explained in detail.

In Chapter 2, the theory fundamentals are settled for Fabry-Pérot fiber-optic interferometric sensors, for photoacoustics theory and photoacoustic image reconstruction.

In Chapter 3, the methods used for this thesis are explained. Some simulations are done to familiarize with the image reconstruction algorithm. Next, it is explained how PVA phantom tissues were prepared as well as the experimental setups correspondent to the experiments. Finally, the photoacoustic image reconstruction process is explained.

In Chapter 4, the results from the experimental setups in Chapter 3, are shown. In Chapter 5, the conclusions and the future work related to this thesis, are discussed.

Chapter 2

Theory Fundamentals

On this chapter, the theory fundamentals will be explained according to the specific goals of this work. First, information on the theory behind a commercial extrinsic Fabry-Pérot interferometric sensor is given. This sensor will be evaluated for the detection of acoustic signals generated by the photoacoustic effect explained in Chapter 1. Next, the photoacoustics theory will be explained in detail. From the coupling of governing equations which describe the effect, to the wave equation solutions for a layer geometry. This layer geometry conveys photoacoustic signal detection in one and/or two dimensions which lead to a photoacoustic tomography and how gold nanoparticles can function as contrast agents.

2.1 Extrinsic Fabry-Pérot Interferometric Sensors

2.1.1 Principle of operation

In a Fabry-Pérot (FP) fiber-optic interferometer, a cavity length is designed so multiple reflected light at certain wavelength enters in resonance inside it. The cavity inside an optical fiber can be built by placing reflective interfaces (mirrors, mirror-like materials, thin films, etc.), or by splicing pieces of optical fiber with different characteristics (e.g. with different refractive index).

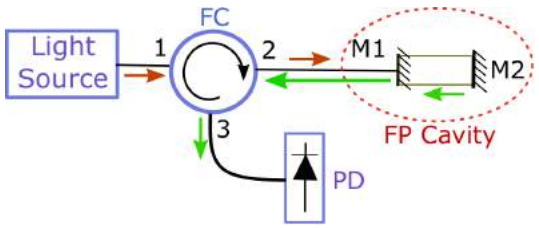

Figure 2.1: Setup of a Fabry-Pérot Interferometer in an optical fiber

In addition, the cavity may change its optical length due to external perturbations (exposure to thermal or pressure waves). Consequently, the resonance wavelength inside the cavity changes. The scheme of a common setup is shown in Fig. 2.1.

A fiber circulator (FC) is placed between a scanning light source and the cavity to guide the ligth towards the interferometer (orange arrows) and to avoid reflections on the light source. Once the light reaches the cavity it is splitted in a reflected and transmitted beam on the first mirror (M_1). The transmitted beam enters the cavity where multiple beams are formed due to multiple reflections on both mirrors (M_1 and M_2). Multiple beams at the output (mirror M_1) are guided (green arrows) to produce an interference signal, often acquired by a photodetecting device (PD) or an optical spectrum analyzer [**?**].

2.1.2 Extrinsic Fabry-Pérot Interferometric Hydrophones

In this section, the fundamental theory followed in the manufacturing process for the hydrophone used for the experiments on this thesis, is explained. The tip of the fiber containing the interferometer for this hydrophone is depicted in 2.2.

A Fiber-Optic Hydrophone System controlled by software, contains a 5mW tunable laser which constantly sweeps its wavelength along a 40nm-span between 1528nm and 1568nm in order to be tuned into the resonance wavelength of the cavity. Also, a photodetection device is included to convert the optical reflected signal to an electrical signal corresponding to the differential change in optical path inside the cavity.

The mirrors which form the hydrophone sensing cavity, M_1 and M_2, are made of gold

thin-films which have been designed to have reflectances of $R_1 = 75\ \%$ and $R_2 = 98\ \%$, respectively. Between the mirrors, a Parylene-C spacer is placed. This polymer changes its length in proportion to the amplitude of an incident pressure wave modifying the relative phase ϕ between multiple reflected beams. Consequently, the normalized total reflected irradiance R at the wavelength λ tuned in the interrogation unit (by the scanning fiber-optic laser enclosed in the hydrophone system) allows to do a follow-up to the pressure changes at the output of the system.

Using the total reflectance equation in a Fabry-Pérot cavity (Eq. 2.1). The transfer function (TF) of a multiple-reflection interferometer is given by

$$R(\phi) = 1 - \frac{(1 - R_1)(1 - R_2)}{\left(1 - \sqrt{R_1 R_2}\right)^2 + 4\sqrt{R_1 R_2}\sin^2\frac{\phi}{2}}, \tag{2.1}$$

where

$$\phi = \frac{4\pi}{\lambda} n l(p), \tag{2.2}$$

λ is the transducer scanning wavelength, n and $l(p)$ are the polymer refractive index and cavity length dependent on the incident pressure, respectively. The sensor used for the experiments in this work is explained in detail elsewhere [54].

The acoustic transduction mechanism uses an optimally biased phase value, ob-

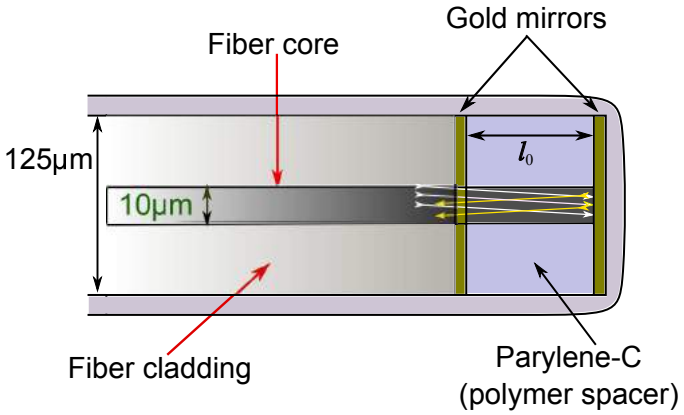

Figure 2.2: Design of the hydrophone with extrinsic FP interferometer built on fiber tip.

tained from considering the corresponding phase to the peak derivative of TF. This works as the inflection point at which the sensor is biased. Being inside this region, and along the linear slope value, guarantees that the detector will be working above its detection threshold and below its quadrature point. Under the optimal biasing conditions, the acoustically induced phase shift $d\phi$ can be considered as being linearly changing the reflectance $R(\phi)$.

The sensor sensitivity is defined as the derivative of the reflectance $R(\phi)$ with respect to the pressure (the change in reflectance generated by an incident acoustic wave),

$$\frac{dR(\phi)}{dp} = \frac{dR(\phi)}{d\phi}\frac{d\phi}{dp}. \tag{2.3}$$

The phase shift resulting from the incident pressure wave in Parylene-C is

$$\frac{d\phi}{dp} = \frac{4\pi n}{\lambda}\frac{l_0}{E}, \tag{2.4}$$

where E stands for the Young's modulus and l_0 is the initial spacer length.

A numerical simulation is made in order to observe the limits between which the hydrophone will be transducing correctly the pressure changes into phase changes, see Fig. 2.3.

On Fig. 2.4, the numerical simulation includes pressure changes applied to the hydrophone, translated into shifts in wavelength. The original transfer function remains drawn in red. The first derivative is drawn as the dashed black line. The black vertical line, indicate the peak value of the first derivative for the original transfer function. The shifted transfer function colored lines with their respective shifted first derivatives will result in a new region for correct transducing. The scanning laser encounters this shifts and tunes a new resonating wavelength when the incident pressure changes the length in the interferometer cavity.

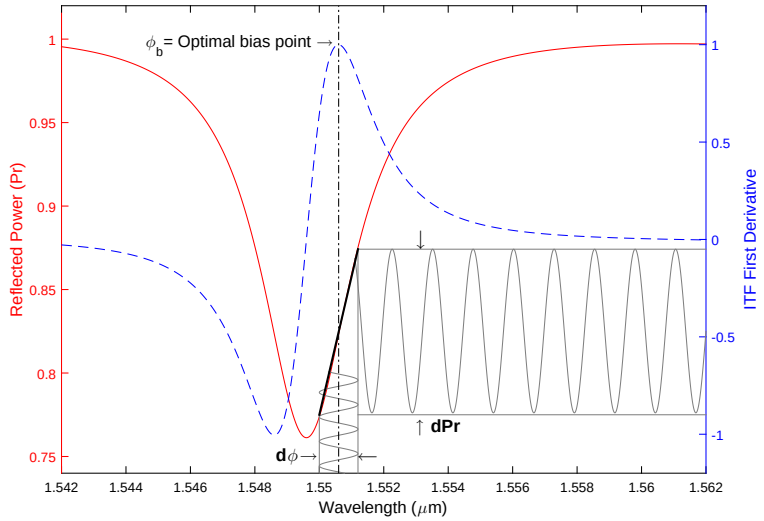

Figure 2.3: Hydrophone Interferometer Transfer Function

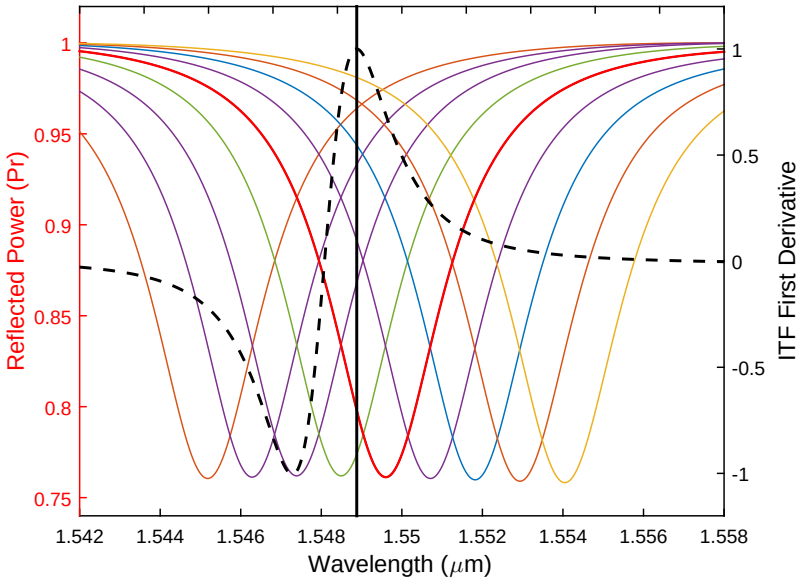

Figure 2.4: Hydrophone Interferometer Transfer Function (Pressure changes applied)

2.2 Photoacoustics Theory

One of the approximations to model the acoustic wave that results from the thermal expansion of a material, is directly related to what happens when a fluid body receives optical radiation. This leads to modelling the acoustic wave generated by simple

geometries, e.g. a layer.

The features of photoacoustic waves analyzed in time domain, and which are emitted by short laser pulse radiation, provide information on the geometry of the body, and the density and sound speed of the body relative to the fluid that is surrounding it.

For long laser pulses, the shape of the photoacoustic wave depends on the symmetry of the body and the intensity profile of the excitation pulse [55].

The problem of solving a photoacoustic wave is approached in [55] as the coupling of equations for both, pressure and temperature. This aproach works similar to the Thermal Piston Model explained in Section 1.6. In the following sections, the solutions for layer geometry are explained for short optical pulses (integral mehtod) and solving the wave equation in the frequency domain.

2.2.1 Temperature-Pressure Equations Coupling

Temperature and pressure variation (differential) equations are coupled to solve the wave equation. This is made to include both equations contributions to the solution. In this equations, γ is the specific heat ratio, α is the pressure expansion coefficient (respect to temperature at constant volume), and H is the energy per unit volume and time deposited by the optical radiation beam.

$$\frac{\partial}{\partial t}\left(T - \frac{\gamma - 1}{\gamma\alpha}p\right) = \frac{K}{\rho C_p}\nabla^2 T + \frac{H}{\rho C_p} \tag{2.5}$$

$$\left[\nabla^2 - \frac{\gamma}{v^2}\frac{\partial^2}{\partial t^2}\right]p = -\frac{\alpha\gamma}{v^2}\frac{\partial^2}{\partial t^2}T \tag{2.6}$$

Before decoupling these equations, it can be seen that Eq. 2.5 is similar to the one for heat diffusion but adding a pressure-dependent term correspondent to adiabatic heating due to compression. Eq. 2.6, on the other hand, describes the acoustic pressure with isothermal sound speed and which is governed by the temperature change rate experienced.

Approximating γ to unity (common approximation for fluids), and considering the heat conductivity to be zero, Eq. 2.5 can be subtituted into Eq. 2.6 to obtain the rigourous wave equation for pressure in the time-domain and without acoustic attenuation (2.7). It is explicitly assumed a homogenous elastic medium to consider it the general photoacoustic (PA) wave equation [56].

$$\left[\nabla^2 - \frac{1}{v^2}\frac{\partial}{\partial t^2}\right] p = -\frac{\beta}{C_p}\frac{\partial H}{\partial t} \tag{2.7}$$

The assumption that the heat conductivity is zero takes place when the acoustic pulse is produced before the sample is significantly heaten by the optical radiation. Also, when the thermal expansion is greater than zero, and the heat conduction is zero, then the absorption of the optical energy would produce an irreversible increase in the volume.

To simplify some calculations, it is often preferred to solve the photoacoustic wave equation for velocity potential, instead of acoustic pressure. This can be derived from Eq. 2.7, and both the instantaneous acoustic pressure p and the particle velocity $\boldsymbol{u}$ can be determined from the following relations:

$$\mathbf{u}(x,y,z) = \nabla\phi \text{ and } p = -\rho\frac{\partial\phi}{\partial t} \quad \therefore \quad \left[\nabla^2 - \frac{1}{v^2}\frac{\partial}{\partial t^2}\right]\phi = \frac{\beta}{\rho C_p}H \tag{2.8}$$

where ϕ stands for the *velocity potencial*.

2.2.2 Integral Solutions for Short Optical Pulses

When solving the wave equation, the Green's functions can be used to obtain an integral solution. The velocity potential used in the previous section can be solved for an infinite space (with densities and sound speed identical for the fluid and the excited sample) as follows (Eq. 2.9):

$$\phi(\mathbf{x},t) = -\frac{\beta}{4\pi\rho C_p}\int_0^t dt' \int g(\mathbf{x},t|\mathbf{x'},\mathbf{t'})H(\mathbf{x'},t)d\mathbf{x'} \tag{2.9}$$

This equation is then applied to the desired geometry adjusting the appropriate Green function to the problem and the number of dimensions in which symmetry is present.

2.2.2.1 Layer Geometry

Given the nature of this project, and the geometry of the samples analyzed for the determination of acoustic waves, the layer geometry allows to have information in two dimensions, whether it is an image, or a set of images for a three-dimensional sample. For a one-dimension symmetry problem, the appropiate Green's function used by Wang et al. in [55], written in Cartesian coordinates is shown in Eq. 2.10, for $z > z'$.

$$g(\mathbf{z}, t|\mathbf{z'}, \mathbf{t'}) = 2\pi v_s \left\{1 - \mathbf{u}[(z - z')/v_s - (t - t')]\right\} \tag{2.10}$$

Here, z' stands for the z-axes points contained inside the thickness of the sample $(-l/2, l/2)$, and $\boldsymbol{u}$ is the Heaviside function.

In addition, the heating function (Eq. 2.11) is defined for a problem of an infinite, optically thin layer in the xy plane with thickness l centered at $z = 0$. It is considered to have an optical absorption coefficient μ_a and heated by a delta function optical pulse with a fluence F (as energy per unit area). A square function $\hat{\Theta}$ is included to define the space in the z-axis in which the heating function takes place. The heating function is then substitued into Eq. 2.9 to obtain Eq. 2.12.

$$H(z, t) = \mu_a F \delta(t) \hat{\Theta}_{-l/2, l/2}(z) \tag{2.11}$$

$$\phi(\mathbf{x}, t) = -\frac{\mu_a \beta F v_s}{2\rho_f C_p} \int_{-l/2}^{l/2} [1 - u(z - z' - v_s t)] dz' \tag{2.12}$$

A retarded time $\hat{\tau}$ with no dimensions is defined in Eq.(2.13) from the edge of the layer to integrate Eq. 2.12. The boundaries for this retarded time are found substituting z with the limits of the integral solved $(-l/2, l/2)$. The result integration respect to z',

can be translated into a group of solutions for the velocity potential where the z' limits become retarded time $\hat{\tau}$ limits. The range of solutions of Eq. 2.13 then goes from 0 to 2 inside the layer thickness, and the group of solutions in terms of z' and $\hat{\tau}$ will have the form of Eq.2.14.

$$\hat{\tau} = \frac{2v_s}{l}\left(t - \frac{z - l/2}{v_s}\right) \tag{2.13}$$

$$\phi(z,\hat{\tau}) = \begin{cases} 0 & \hat{\tau} < 0 \\ -\frac{\mu_a \beta F v_s (l/2)}{2\rho C_p}\hat{\tau} & 0 < \hat{\tau} < 2 \\ -\frac{\mu_a \beta F v_s l}{2\rho C_p} & \hat{\tau} > 2 \end{cases} \tag{2.14}$$

The model of the velocity potential for the layer can be used to recover the photoacoustic pressure from Eq. 2.8, and which describes a square-wave pressure pulse (Eq. 2.15) travelling along the positive z-axis (forward). There is also a compressive pulse propagating along the negative z-axis (backwards) when ϕ is evaluated in $z < z'$.

$$p(t) = -\rho\frac{\partial\phi}{\partial t} \rightarrow p(\hat{\tau}) = -\frac{2\rho_f v_s}{l}\frac{\partial\phi}{\partial\hat{\tau}} \quad \therefore \quad p(\hat{\tau}) = \frac{\mu_a \beta F v_s^2}{2C_P}\hat{\Theta}_{0,2}(\hat{\tau}) \tag{2.15}$$

$$p(z,t) = \frac{\beta v_s}{2C_P}\int H\left(z', t - \frac{z - z'}{v_s}\right)dz' \tag{2.16}$$

For applications where photoacoustic pressure signals are seeked in one dimension, it is also acceptable to derivate Eq. 2.12 in time. The laser beam heating function for this case would be integrated in the retarded time, as shown in Eq. 2.16. However, even though the heating function can be modelled according to the geometry of the laser beam profile, this is still a limited solution for the PA wave when the coupling impedances between the interfaces sample-fluid are not considered. In the following section, an alternative solution is presented.

2.2.3 Frequency Domain Solution to the Wave Equation

Another approach to solve the wave equation arises from the assumption that, both the pressure and the heating function are sinusoidal functions in time. The main advantage of solving the wave equation in the frequency domain is the ability to find solutions to the photoacoustic effect when the optically absorbing sample and the surrounding fluid (ideally acoustically transparent) have different densitites and sound speeds. As to compare the solutions, a layer geometry will also be solved for the same characteristics as the one presented in the previous section.

2.2.3.1 Layer Geometry

An infinite fluid layer is considered for the problem. It lies in the xy plane with thickness l, and centered at $z = 0$. This time, the heating function (Eq. 2.17) is defined using only the thermal expansion coefficient, the optical absorption coefficient, and the optical beam profile directed along the z-axis. The beam is intensity-modulated at a frequency ω. The variation of the pressure is expressed as $exp(-i\omega t)$.

$$H(z,t) = \mu_a I_0 e^{-i\omega t} \tag{2.17}$$

There is a reduction from a partial differential equation made in time and space to a Helmholtz equation just for the space variable, which results in pressures inside and outside the layer (Eq. 2.18) and where k stands for the wave number.

$$(\nabla^2 + k^2)p = \begin{cases} \frac{i\mu_a\omega\beta I_0}{C_P}, & z \geq 0 \\ 0, & z \leq 0 \end{cases} \tag{2.18}$$

Different to the integral solution approach, one of the solutions to the Helmholtz equation is limited to the space inside the layer, where plane waves are considered to be travelling in a left or a right-going direction in addition to a solution to the inhomogeneous equation. Inside the layer, the spatial component in Eq. 2.17 is a

constant, so the inhomogeneous solution should be a dimensionless constant multiplied by a pressure term (Eq. 2.19). On the other hand, outside the layer, there are also right or left-going travelling waves propagating along the positive (P_R) or the negative (P_L) z-axis, respectively. In the following equations (Eqns. 2.20), the sub-index in the wave number indicates whether the wave is propagating inside the layer (k_l), or outside the layer (in the fluid, k_f).

$$\left(\frac{i\mu_a\beta I_0}{\rho_l v_s^2}\right)\rho_l v_s^2 \tag{2.19}$$

$$p = \left(1 + \hat{P}_1 e^{ik_l z} + \hat{P}_2 e^{-ik_l z}\right) e^{-i\omega t} \tag{2.20}$$

$$p_R = \hat{P}_R e^{i\left[k_f(z-l/2)-i\omega t\right]} \tag{2.21}$$

$$p_L = \hat{P}_L e^{i\left[k_f(z+l/2)+i\omega t\right]} \tag{2.22}$$

The solutions shown above present four different unknown constants, where, by symmetry, $\hat{P}_1$ is equal than $\hat{P}_2$, and $\hat{P}_R(z)$ is equal than $\hat{P}_L(-z)$. Following the principles of linear acoustics, the pressure and coordinate, or any of its time derivatives, must be continuous at an interface. For PA waves, the gradient of the pressure divided by the density is equal to the a negative acceleration, so the boundary conditions will be as follows:

$$p_f = p_l \quad \therefore \quad \frac{\nabla p_f}{\rho_f} = \frac{\nabla p_l}{\rho_l} \tag{2.23}$$

For the layer problem in question, the gradient of the pressure is the derivative with respect to the z-coordinate where the layer exists. Here, dimensionless parameters $\hat{\rho}$ and $\hat{c}$ are defined for simplicity:

$$\hat{\rho} = \frac{\rho_l}{\rho_f} \quad \text{and} \quad \hat{c} = \frac{v_s^l}{v_s^f} \tag{2.24}$$

$$\nabla p_l = \frac{\partial p}{\partial z} \quad \rightarrow \quad \hat{P}_R = 1 + \hat{P}_1 e^{ik_l l/2} + \hat{P}_1 e^{-ik_l l/2} \tag{2.25}$$

$$\hat{\rho}\hat{c}\hat{P}_R = \hat{P}_1 e^{ik_l l/2} - \hat{P}_1 e^{-ik_l l/2} \tag{2.26}$$

A dimensionless frequency parameter $\hat{q}$ and a similar term for retarded time than the one used in the integral solution is shown in (Eq. 2.27). To obtain the photoacoustic pressure outside the layer, Eqs. 2.25 and 2.26 are solved for $\hat{P}_1$ and $\hat{P}_R$.

$$\hat{q} = \frac{\omega l}{2v_s^l} \quad and \quad \hat{\tau} = \frac{2v_s l}{l}\left(t - \frac{z - l/2}{v_s^f}\right) \tag{2.27}$$

The solved equation for the frequency domain is:

$$p_R(\hat{q}) = \frac{i\mu_a \beta I_0 v_s^l l}{2C_P}\left(\frac{sinc\hat{q}}{\sin\hat{q} + i\hat{\rho}\hat{c}\cos\hat{q}}\right) e^{-i\hat{q}\hat{\tau}} \tag{2.28}$$

If a delta function is used as a heating pulse, the time-domain pressure can be found applying the Fourier transform to Eq. 2.28. The dimensions have to be corrected to have a dimensionless integral multiplied by a prefactor with units of pressure as seen in Eq. 2.29.

$$p_R(\hat{\tau}) = \frac{i\mu_a \beta F v_s^{12} l}{2\pi C_P}\int_{-\infty}^{\infty}\left(\frac{\mathrm{sinc}\hat{q}}{\sin\hat{q} + i\hat{\rho}\hat{c}\cos\hat{q}}\right) e^{-i\hat{q}\hat{\tau}} d\hat{q} \tag{2.29}$$

Given this solutions for the photoacoustic wave equation, the theory can be applied to reconstruct images depending on the geometry analyzed. In the following section, two main algorithms to solve the photoacoustic inverse problem of image reconstruction are explained.

2.2.4 Photoacoustic Tomography with Contrast Agents

In this project, one of the specific goals is to test the advantage of using contrast agents for photoacoustic signal detection and photoacoustic tomography. In the following section, it is stated how gold nanoparticles can work as anisotropic contrast agents with spectral selectivity.

2.2.4.1 Gold Nanoparticles as Contrast Agents

Gold nanoparticles are used as the contrast agent for signal enhancement and for time-intensity curve (TIC) measurements. Gold nanoparticles exhibit strong photoacoustic (PA) responses and have been considered relatively safe for various biomedical applications.

Because it has been shown that the PA signal amplitude of gold nanoparticles is linearly proportional to the concentration, by recording the signal amplitude as a function of time (i.e., the TIC), flow information can be extracted. Gold nanoparticles exhibit a strong response from the visible to infrared spectral region.

Therefore, gold nanoparticles effectively assist the generation of PA signals. In photoacoustic imaging, gold nanoparticles have been used for contrast enhancement for tumor detection and rat brain imaging. In addition, PA molecular imaging of tumor cells using bioconjugated gold nanoparticles for specifc targeting has also been demonstrated.

The absorption spectrum of gold nanoparticles is associated with surface plasma resonance, which is both size- and shape-dependent. The peak absorption wavelength weakly depends on the diameter of gold nanoparticles, but strongly depends on the aspect ratio (defined as the ratio of the length of the major axis to that of the minor axis). Thus, choosing an irradiating wavelength corresponding to the maximum optical absorption of the gold nanoparticles can effectively enhance the generation of the PA signal. As an example, Figure 2.5 shows that the absorbance peak amplitude of nanoparticles when illuminated at an 808nm wavelength, and at different intensities.

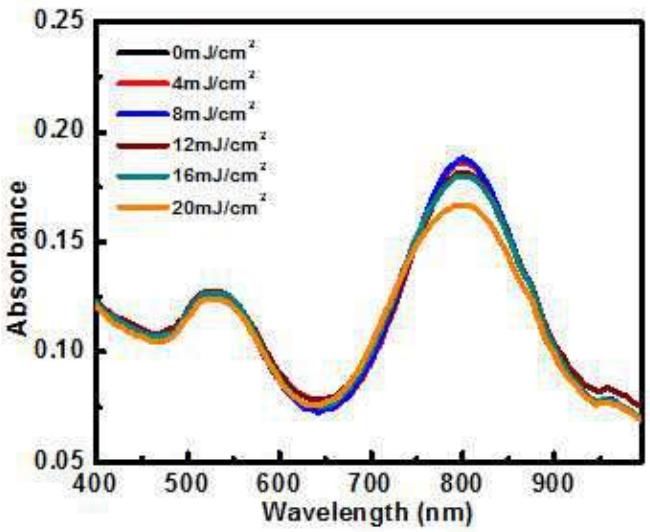

Figure 2.5: Absorbance of nanoparticles to different light intensities

2.3 Photoacoustic Image Reconstruction

Image reconstruction of photoacoustic signals is mainly used for photoacoustic tomography (PAT). The reconstruction is made from an internal pressure distribution detected with small-aperture ultrasound detectors [55]. As explained before, the acoustic source is produced by the thermal expansion (temperature increase) that an absorption center experiences due to radiation of pulsed light. The main application for PAT is on biomedical imaging, where the combination of the ultrasonic resolution and optical contrast result in a strong advantage over other imaging techniques. In this section, the time reversal reconstruction algorithm is explained.

2.3.1 Time Reversal in Photoacoustic Tomography

Reconstruction methods are still being developed and studied, but in order to derive an algorithm, the specific detection geometry must be controlled and so, the physics behind an exact reconstruction will model specific algorithms for a few special geometries. Currently, there are not available methods to reconstruct an initial distribution directly from the signal detected across a surface. Energy-deposition plays an important role at

this point, by being equivalent to the initial pressure distribution. This is how energy-deposition in Thermoacoustic Tomography (TAT) is introduced as the first approach towards image reconstruction through the Time Reversal method.

First, a thermoacoustic wave equation is defined in a very similar manner than the one for photoacoustics. The heating function defined for PA, is now called energy-deposition function. For this case, Eq. 2.7, is redefined to have Eq. 2.30. The energy-deposition function is in Eq. 2.31 where $\eta(t)$ describes the irradiating pulse shape in time-domain, and $A_e(\mathbf{r})$ describes the microwave absorption properties in a medium $\mathbf{r}$.

A delta pulse is considered as pulse profile shape and Eq. 2.30 is integrated twice over infinetely small real positive (negative) values of time, in other words, t over $[0-,(0+)]$. A new equation for p_f is given, where it is assumed that the thermoacoustic pressure is finite, and which means that reconstruction in TAT is equivalent to reverting the pressure field to time zero (Eq. 2.32).

$$\nabla^2 p_f(\mathbf{r},t) - \frac{1}{v_s^2}\frac{\partial p_f(\mathbf{r},t)}{\partial t^2} = -\frac{\beta}{C_v}\frac{\partial H(\mathbf{r},t)}{\partial t} \tag{2.30}$$

$$H(\mathbf{r},t) = I_0\eta(t)A_e(\mathbf{r}) \tag{2.31}$$

$$p_f(\mathbf{r},0+) = \frac{\beta v_s^2 I_0}{C_v}A_e(\mathbf{r}) \tag{2.32}$$

The time reversal algorithm works in the time domain and it takes the advantage of the reversibility of the wave equation in a lossless (non-dissipative) medium to find a back-propagation field from a measured forward-propagation field, once the initial pressure source has been removed.

For anomaly detection purposes, the detection is done on a surface that surrounds the anomaly, where either the acoustic wave reflected or the transmitted (through a medium of immersion), are taken to make a time-reversed chronology. Now, the detected pressure set of data will travel back to locating the anomaly in time [57]. The wave equation experiences the time variable transformation $t \longrightarrow -t$.

$$\Delta p_f(\mathbf{r},t) - \frac{1}{v_s^2}\frac{\partial^2 p_f(\mathbf{r},t)}{\partial t^2} = q(\mathbf{r},t) \tag{2.33}$$

2.3.2 PAI Reconstruction with MATLAB k-Wave Toolbox

For this work, the image reconstruction will be performed by an algorithm written in MATLAB. In this, functions from the k-Wave Toolbox for Acoustic Fields, will be used to obtain an image from a set of acquired pressure signals generated by an illuminated sample.

In the classical case of a small amplitude acoustic wave propagating through a homogeneous and lossless fluid medium, the first-order governing equations are given by

$$\begin{aligned} \tfrac{\partial \mathbf{u}}{\partial t} &= -\tfrac{1}{\rho_0}\nabla p \\ \tfrac{\partial \rho}{\partial t} &= -\rho_0 \nabla \cdot \mathbf{u} \\ p &= c_0^2 \rho \end{aligned} \tag{2.34}$$

where $\mathbf{u}$ is the acoustic particle velocity, p is the acoustic pressure, ρ is the acoustic medium density, ρ_0 is the equilibrium density, and c_0 is isentropic the sound speed. When these equations are combined together, they give the familiar second-order wave equation

$$\nabla^2 p - \frac{1}{c_0^2}\frac{\partial^2 p}{\partial t^2} = 0 \tag{2.35}$$

The main simulation functions in k-Wave (`kspaceFirstOrder1D`, `kspaceFirstOrder2D`, `kspaceFirstOrder3D`) solve the coupled first-order system of equations rather than the equivalent second-order equation. It allows both mass and force sources to be easily included into the discrete equations. Also, it allows the use of a special anisotropic layer (known as a perfectly matched layer or PML) for absorbing the acoustic waves when they reach the edges of the computational domain. Finally, the calculation of the particle velocity allows quantities such as the acoustic intensity to be calculated. This

is useful, for example, when modelling how ultrasound heats biological tissue due to acoustic absorption.

When acoustic absorption and heterogeneities in the material parameters are included, the system of coupled first-order partial differential equations changes and includes an acoustic particle displacement term and an operator which include acoustic absorption and dispersion parameters.

2.3.2.1 Acoustic Source Terms

The equations given in the previous section describe how acoustic waves propagate under various conditions, but they don't describe how these waves are generated or added to the medium. Theoretically, linear sources could be realised by adding a source term to any of the equations of mass, momentum, or energy conservation. For example, adding a source term to the momentum and mass conservation equations describing linear wave propagation in a homogeneous medium gives

$$\begin{aligned} \tfrac{\partial \mathbf{u}}{\partial t} &= -\tfrac{1}{\rho_0}\nabla p + S_F \quad , \quad \text{(momentum conservation)} \\ \tfrac{\partial \rho}{\partial t} &= -\rho_0 \nabla \cdot \mathbf{u} + S_M \quad , \quad \text{(mass conservation)} \\ p &= c_0^2 \rho \quad \text{(pressure-density relation)} \end{aligned} \tag{2.36}$$

Here S_F is a force source term and represents the input of body forces per unit mass in units of N kg^{-1} or m s^{-2}. S_M is a mass source term and represents the time rate of the input of mass per unit volume in units of kg $m^{-3}s^{-1}$ (the term S_M/ρ_0 in units of s^{-1} is sometimes called the volume velocity). In the corresponding second-order wave equation, the source terms appear as

$$\nabla^2 p - \frac{1}{c_0^2}\frac{\partial^2 p}{\partial t^2} = \rho_0 \nabla \cdot S_F - \frac{\partial}{\partial t} S_M \tag{2.37}$$

This illustrates that it is actually the spatial gradient of the applied force, and the time rate of change of the rate of mass injection (volumetric acceleration) that give rise to sound.

2.3.2.2 The k-space pseudoespectral method

The best approach for discretising a particular problem depends on many factors. For example, the size of the computational domain, the number of frequencies of interest, the properties of the medium, the types of boundary conditions, and so on. Here, we are interested in the time domain solution of the wave equation for broadband acoustic waves in heterogeneous media.

The drawback with classical finite difference and finite element approaches for solving this type of problem is that at least 10 grid points per acoustic wavelength are generally required to achieve a useful level of accuracy (a level of accuracy on a par with the uncertainty in the user-defined inputs).

To reduce the memory and number of time steps required for accurate simulations, k-Wave solves the system of coupled acoustic equations described in the previous sections using the k-space pseudospectral method (or k-space method).

This combines the spectral calculation of spatial derivatives (in this case using the Fourier collocation method) with a temporal propagator expressed in the spatial frequency domain or k-space. In a standard finite difference scheme, spatial gradients are computed locally based on the function values at neighbouring grid points

The photoacoustic image reconstruction algorithm in the MATLAB program needs five concepts to be defined: the computational grid, the acoustic medium, the sensor array geometry (and number of sensors), the time array for reconstruction and the pressure distribution source to be reconstructed.

2.4 Chapter Conclusions

Once the theory on the extrinsic sensing device has been explained, it is now possible to understand how it works and test its performance for acoustic wave detection. The principle operation of a Fabry-Pérot interferometer inside an optical fiber allows to have one or more cavities to monitor perturbations of different nature, and for this

case, one cavity sensing incident ultrasound waves. The high sensitivity provided by optical sensing devices, make these hydrophones an interesting alternative to detect acoustic signals with the advantages of optical fibers.

In Chapter 3, the methods for testing the device include the detection of a signal when different materials are illuminated (excited). The photoacoustic image reconstruction will be explained in detail for a specific experimental setup to perform a two-dimensional circular scan of a sample.

Chapter 3

Methods

In this chapter, the methods for this thesis are presented. Simulations for acoustic waves in one and two dimensions are presented with the considerations of the k-wave MATLAB Toolbox explained in Chapter 2.

The hydrophones will be tested by illuminating different samples and detecting the acoustic signal generated. This allows to determine either their thickness or the characteristic speed of sound in those samples. With the purpose of approaching the experiments to a biomedical imaging application, skin-like phantom tissues will be prepared and the process the preparation will be explained.

The experimental setup for measurement of thickness and experiments with phantom tissues are revealed in this chapter followed by a multi-point signal detection experiment. From this last experiment, a photoacoustic image reconstruction will be performed by introducing the recovered data to a reconstruction algorithm.

3.1 Simulations of Acoustic Fields with MATLAB k-Wave Toolbox

Simulations are made for an initial value problem. An initial pressure distribution is given to simulate the propagation of acoustic waves in a specific medium. In the

following subsections, examples of one-dimensional and two-dimensional simulations for acquiring pressure signals inside an acoustic field.

3.1.1 Simulation of obtects (1D)

For a one dimension example, brought by the toolbox package in [58], an initial pressure distribution is given. Some other parameters are given (density and speed of sound), which change of value at some point of the distance dimension established for this simulation. Figure 3.1, shows the initial parameters introduced to the algorithm before it is executed. The line sensors' positions are also given. Once executed, the example

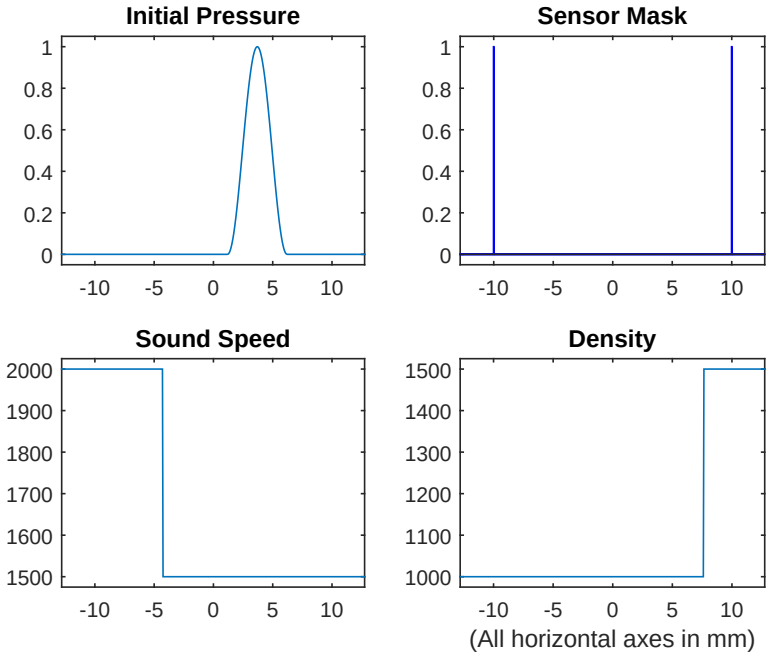

Figure 3.1: Initial Simulation Conditions

shows the pressure signals acquired by the linear sensors. The simulation results can be observed in Fig. 3.2.

In the next subsection, a two-dimensional example is modified so that the initial pressure is given and a reconstruction algorithm is applied.

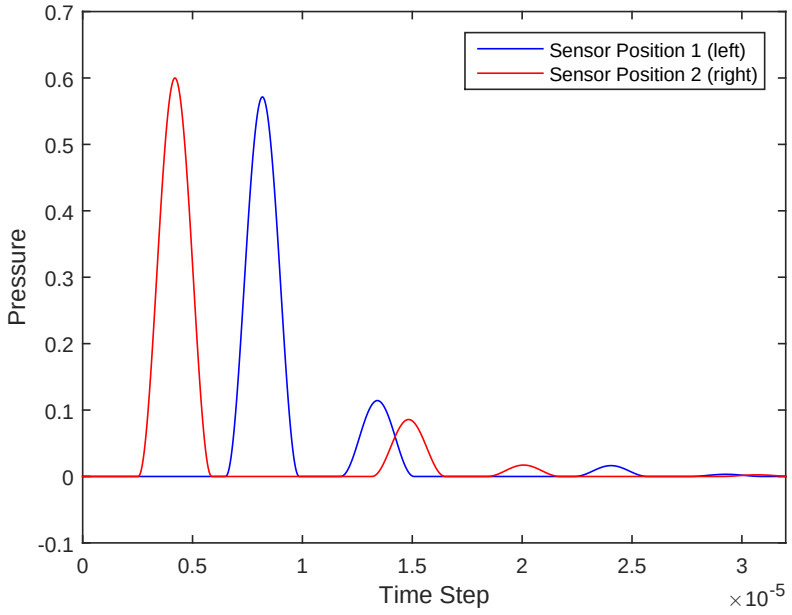

Figure 3.2: Signals detected by line sensors

3.1.2 Simulation of objects (2D)

An array of 180 point detectors lay around the pressure source to make a circular scan of the acoustic field generated by the source. The results from the scan form a pressure matrix (pressogram) showing the acoustic pressure signal detected by each point detector. This pressogram is later introduced to reconstruct the initial pressure distribution by means of either the back-projection algorithm (explained in section **??**) or the time reversal algorithm (explained in section 2.3.1). The initial pressure distribution along with the point detectors array is depicted in Fig. 3.3. For a constant initial pressure of 1.5 Pa along the vessel-shaped distribution, the resulting pressogram is shown in Fig. 3.4.

For this work, the time reversal algorithm is chosen. The geometries and parameters to be solved by the functions in the toolbox are quite flexible. The simplicity and effectiveness of this algorithm, make it the most suitable option for reconstruction in most cases.

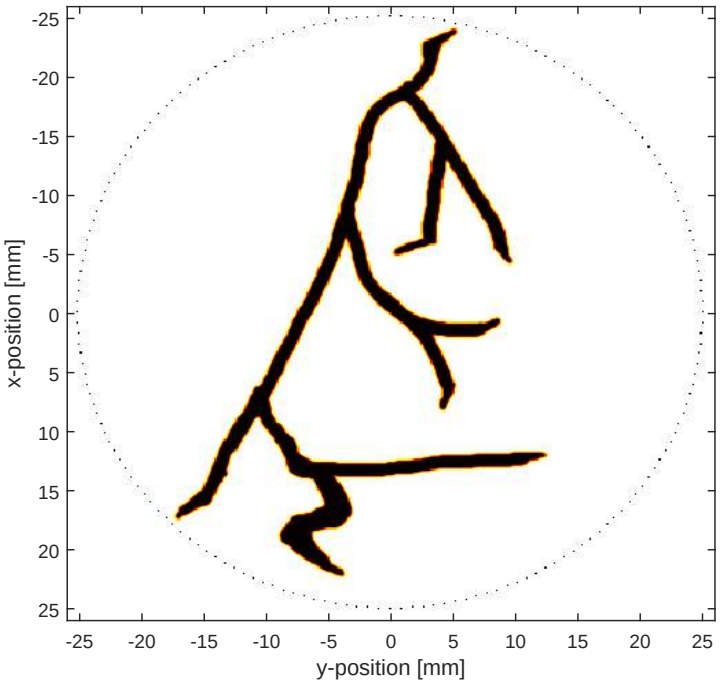

Figure 3.3: Initial Pressure Distribuition and Point Detectors Array

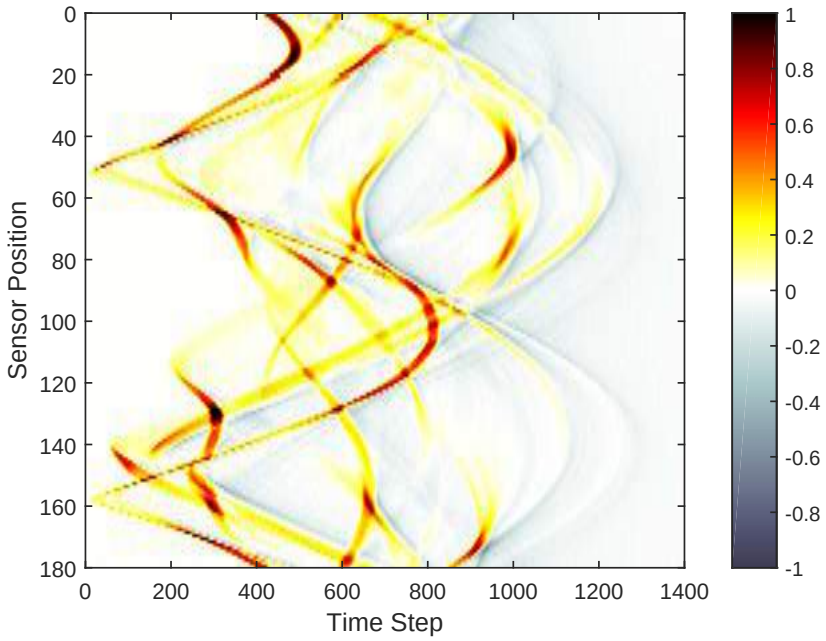

Figure 3.4: Pressure Signals detected by the point detectors array

3.1.3 Time Reversal Algorithm

For the particular case of this initial pressure distribution, two reconstructions are made. The first, depicted in Fig. 3.5a, shows the reconstructed pressure with point detectors. From the first reconstructed data, an interpolation can be done, as shown in Figure 3.5b. In most cases, the emulation of a continuous circular sensor, instead of discrete sensor made with point detectors, improves the visualization and contrast of the image.

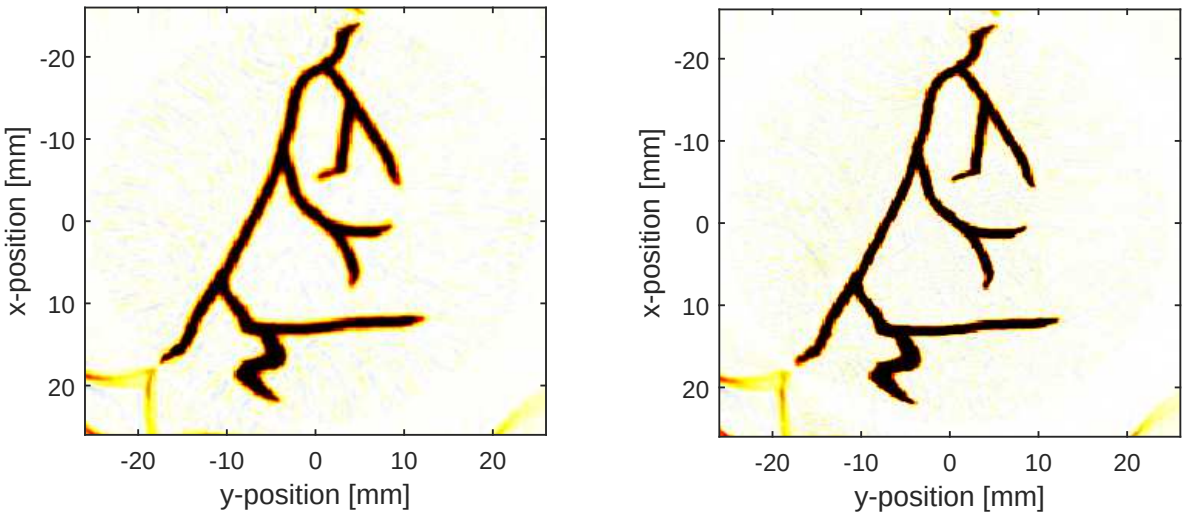

(a) Point Detection

(b) Interpolated Data

Figure 3.5: Reconstruction with Time Reversal Algorithm

The main reason of using an irregular pressure distribution was to test the capability of the algorithm for its use in a real experiment where circular scan produces a pressogram for later reconstruction with this algorithm. However, this is still an ideal distribution introduced, and it virtually detected the signals on each point detector by directly solving first order equations. It also solves them for a space under ideal conditions, with an homogeneous propagation medium, and a given pressure value all along the irregular shape.

3.2 Preparation of Phantom Tissues

Photoacoustics presents itself as a promising technique which main interest nowadays is how it can improve biomedical imaging. In order to emulate a biological tissue, phantom tissues made with polymers can be prepared. In order to determine if anisotropic materials introduced in the tissue improve the photoacoustic signal (contrast) or, if it is dependent to the state of polarization of the excitation light, gold nanoparticles are used. One of the experiments consists on testing the photoacoustic signal detection when the tissue is illuminated with two different states of linearly polarized light In this section, the method for the preparation of polyvinyl-alcohol phantom tissues is presented.

First, a beaker with 190 ml of triple distilled water has to be heated on a hot plate until the water reaches 80°C - 90°C. Once the temperature is reached, a magnetic mixer is introduced in the water to slowly add 15 gr of powdered polyvinyl-alcohol (PVA, Molecular weight = 86,000 - 142,000). The solution has to be mixed for two hours approximately, mantaining the temperature. The beaker has to be covered to partially avoid the evaporation of the water, while the PVA is also completely dissolved.

For the second part of the preparation, the solution is removed from the hot plate and cooled down until it reaches room temperature. Next, the plate is turned on for agitation only, and 1ml of ethylene glycol is added. Once incorporated, the solution keeps mixing and 1ml of an intralipid emulsion is added and mixed to obtain optical scattering properties. Finally, in order to soften the phantom's consistency, 1ml of formaldehyde is added and mixed. Both, the ethylene glycol and the formaldehyde promote the crosslinking of PVA chains.

Third, the final mix is poured into aluminium moulds, 50 milimiters each. It later begins a freezing/thawing process of 12 hours each. The process has to be repeated at least twice, but for this case, four frezzing/thawing processes were experimented by the sample to obtain an optimum consistency.

In the first thaw process, a couple channels will be formed by introducing plastic

filaments of 1.2mm in diameter. The filaments will be extracted on the last thaw process. At this moment, the channels were filled with a mix of 1gr of porcine gelatine dissolved in 10ml of water and 0.4ml of a water solution with gold nanorods (AuNRs) with a longitudinal surface plasmon resonance at (808±15) nm.

Finally, the phantom tissues are separated from the moulds and immersed in distilled water for preservation until they are used.

3.3 Experimental Setups

3.3.1 Measurement of Thickness of Materials (Speed of sound)

3.3.1.1 Rubber Slabs

A square-shaped 3mm-thick rubber sample is illuminated by 5ns-pulse beam at a repetition rate of 10Hz achieved with a pulsed tunable wavelength laser (Optical Parametric Oscillator, OPO) source set at $\lambda = 665nm$.

The energy density applied is $40\text{mJ}/cm^2$. The energy absorption in the sample produces acoustic signals which are later detected by a Fabry-Pérot fiber-optic interferometric ultrasound hydrophone.

The sample and the hydrophone are immersed in a water tank to reduce coupling impedances between the sample and the propagation medium (water) in which the signal will be detected by the hydrophone.

The characteristic sensitivity of each hydrophone used for the performed experiment, allow obtaining signals with different amplitudes observed in the time domain with an oscilloscope.

The trigger signal used for synchronization of the experimental setup was taken from the OPO controller.

The experimental setup is depicted in Fig. 1. Once the acoustic signals are observed, they are later processed by graphic software to measure the peak-to-peak amplitudes for each case. These amplitudes are obtained to compare the inherent sensitivity of each

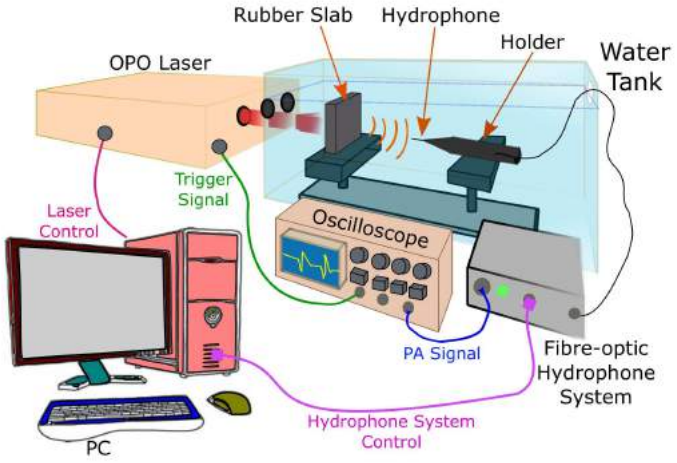

Figure 3.6: Experimental setup for measurement of thickness (rubber slabs)

hydrophone when exposed to the same (acoustic) pressure signal. From these individual responses, it is possible to select the right hydrophone for a specific application, depending on what is the needed sensitivity or how small the detected signal will be.

Both, a rarefaction and a compression signal are expected to be seen derived from the interfaces experiencing changes in impedance due to the nature of the media involved (water-sample/sample-water). The ability to observe and measure this behavior is the starting point towards choosing the accurate transducer for such application.

The separation between these rarefaction and compression signals in the time domain for each transducer gives the necessary information to determine the thickness if the speed of sound of the material is known.

Also, the inverse calculation could be applied to determine the speed of sound in the material if the thickness is given.

3.3.1.2 Aluminum Slabs

Similar to the experimental setup depicted for the rubber samples, aluminum slabs are illuminated with the same beam characteristics, except for its wavelength. For these experiments, the samples are illuminated at $\lambda = 670nm$ to generate an acoustic signal. The slabs had four different thicknesses: 1.5mm, 2.9mm, 3.9mm and 5.9mm.

The same transducer as the one used for rubber samples, detected the acoustic signals as well. The energy density applied is adjusted depending on the attenuation of the acoustic signal detected by the transducer. This is done in order to increase the amplitude of the signal and to improve the visualization of the separation between the signals for these cases. Aluminum samples are expected to produce acoustic signals with

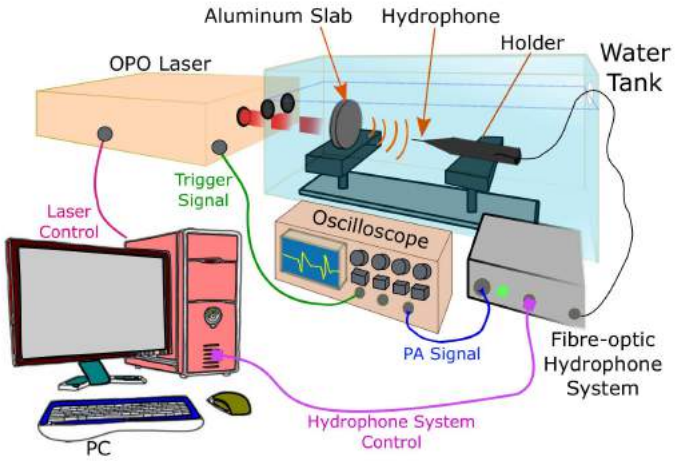

Figure 3.7: Experimental setup for measurement of thickness (aluminium slabs)

higher frequency than the ones for rubber when illuminated due to its characteristic speed of sound and density. In addition, the nature of the sample allows to expect that several reflections will happen inside the slab, and so more than one photoacoustic signal will be seen in the time-domain response, these being attenuated after each reflection.

The separation time between these reflections corresponds to the round-trip time of the acoustic signal inside the slab. In other words, the separation time observed will be the time in which the sound makes two travels inside the slab. Determining either the thickness of the slab or the speed of sound inherent to the aluminum, will be possible, taking these considerations.

3.3.2 Phantom Tissues with Gold Nanoparticles

3.3.2.1 One-sensor signal detection

Phantom tissues were prepared for these experiments as explained in section 3.2. A concentration of gold nanoparticles (nano-rods) immersed in porcine gelatin were deposited in a cylindrical cavity formed inside the polyvinyl-alcohol based phantom tissue. The surface plasmon of the nano-rods experience optical absorption at certain wavelength. The cylindrical cavity containing the nanoparticles has a diameter of 0.75mm approximately. The 1cm-thick phantom tissues are illuminated at $\lambda = 808nm$, correspondent to the surface plasmon optical absorption wavelength. The samples were later illuminated at $\lambda = 665nm$ in order to compare the amplitude of the photoacoustic (PA) signals in time-domain for both cases. PA signals generated by the anisotropic optical absorbers were detected by an interferometric fiber-optic ultrasound transducer (FOUT).

As a part of the setup, two orthogonal linear polarization states are generated by placing of retarding wave plates of $\lambda/2$ in front of the laser beam exit. The linearly polarized beam then illuminates the phantom tissue, causing the nano-rods to absorb the light differently for each polarization state.

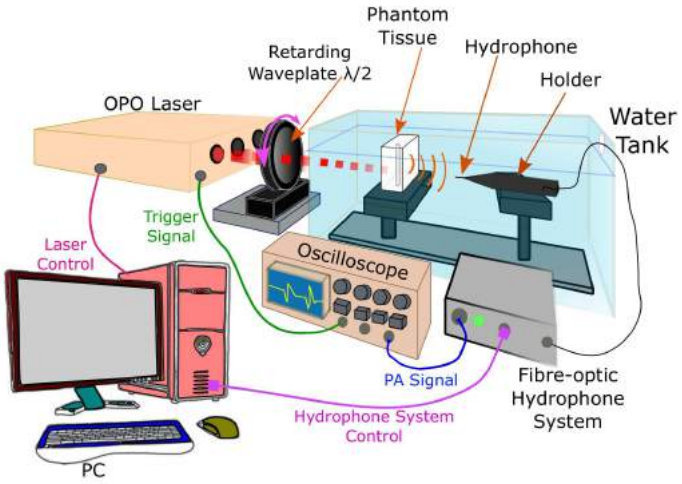

Figure 3.8: Experimental setup to measure PA signals from nanorods channel

In theory, each nano-rod absorbing light will generate an acoustic signal, which, depending on the concentration, will result in a combination of PA signals in time domain, corresponding to the whole response of the area illuminated. The polarization states would produce two response signals which may differ in amplitude and/or in shape.

In order to align the nano-rods inside the cylindrical cavity so they are all oriented at the same direction, the phantom tissue experienced uniaxial tension with a home-made machine. This alignment would allow the nano-rod to be illuminated along its length, instead of along its width. As a result, it increases the absorbing area and consequently, the amplitude of the acoustic signal generated by this absorption.

3.3.3 Multi-point signal detection (2D)

A nickel sample with an external cylindrical shape and an internal semi-squared shape was illuminated with a pulsed tunable wavelength laser (NT352, Ekspla®). A 5 ns-pulsed beam with a repetition rate of 10 Hz was tuned at 700 nm wavelength. Energy per pulse was 35 mJ distributed over a 12 mm-in-diameter spot. The experimental setup for these experiments is depicted in Fig. 3.9

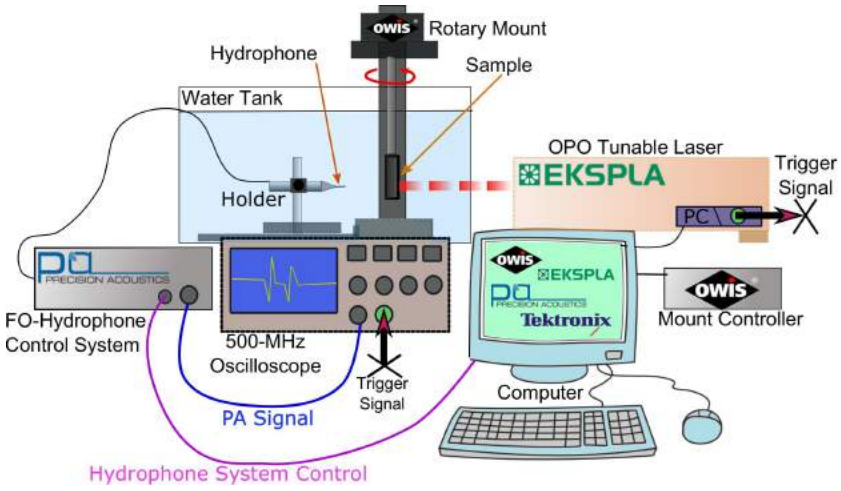

Figure 3.9: Experimental setup

Once the optical absorption by the sample induces a pressure change in the sorrounding fluid, an acoustic signal is generated under thermal confinement and thermo-ellastic regime. A Fabry-Pérot fiber-optic interferometric hydrophone (PAFOH53, Precision Acoustics®) placed 3-cm from the sample is used to detect the acoustic signals. Both, the hydrophone and the nickel sample are immersed in a tank filled with water as the propagation medium. The optical interference signal produced by the Fabry-Perot cavity at the sensing tip of the fiber (photoacoustic signal) was recorded with a Tektronix® TDS3504B oscilloscope. It achieves a 500 MHz-bandwidth that ensures a reliable signal acquisition delivered by the transducer controller (100-MHz band-limited).

A rotary motorized mount (OWIS®) controlled by software is used to achieve 72 measurements in 5-degree steps around the sample. These data are processed to build a matrix of detected time-domain pressure distribution (pressogram), some further processing is done to associate the frequency-domain pressogram to the frequency sensitivity response of the sensor (Fig. 3.10b). The associated input pressogram is later introduced to a MATLAB® program designed for photoacoustic image reconstruction in time reversal mode using functions from the k-Wave Toolbox for acoustic fields. The reconstruction algorithm can be found in detail elsewhere [58]. Features such as density, speed of sound, frequency bandwidth, distribution of sensors and dimensions are defined before running the reconstruction.

3.4 PA Image Reconstruction with MATLAB k-Wave Toolbox

The computational grid was an 800 x 800 pixels plane, corresponding to a 1.8 cm x 1.8 cm plane. The number of pixels determined the maximum frequency that the algorithm can resolve, 33.33 MHz for this case. Knowing the nature of the sample, the acoustic medium was defined for both, for water and nickel, to compare the features identified on both media. The densities were chosen as 1,000 kg/m^3 and 8,903 kg/m^3, and the speeds

of sound were chosen as 1,500 m/s and 3,000 m/s, for water and nickel, respectively.

The time of flight (ToF) between the hydrophone and the edge of the sample was found to be approximately 20 μs, and the one between the edge and the center of the sample (considered to be all nickel) was 3.90 μs. This gives a total of 23.90 μs, from the center of the sample to the hydrophone. However, the region of interest for this work, in the time domain, is the one that offers information on the outer shape (and, if possible, the inner shape) of the sample, so the ToF inside the sample is the reference for choosing a visualization window in the oscilloscope which offers the desired information.

The sensor array lay on a circular shape with a 6 mm radius. The distance from the center corresponded to the spatial point from which the data were acquired. This is related to the start acquisition time set on the oscilloscope. Seventy-two equally-spaced point detectors lay around the scan. For the time array, the oscilloscope span-time chosen was a window of 4 μs, which in theory, shows information on the edge of the sample being illuminated by the pulsed laser, and the data found 3.90 μs from the edge, would correspond to the center of the sample. For this case, 10,000 points are chosen to be recorded per measurement, resulting in time steps of 0.4 ns.

From the acquired data, a two-dimension matrix is formed so it becomes the input pressure distribution (pressogram) to be reconstructed. Each PA signal is treated as explained in Section 3.5.

Figure 3.10 shows the frequency responses used for the treatment. The transfer function of the interferometer (Fig. 3.10a) is deconvoluted from the frequency response of the sensor (Fig. 3.10b).

Running the algorithm displays some of the reconstruction parameters along with a precomputation time and a total expected reconstruction time. The running time is dependent on the computer characteristics. For a computer with an Intel® Xeon® processor, CPU model E5-1620, running at 3.5GHz, the average computation time for the reconstruction was 23 minutes. The resulting matrix is displayed, the axes were adjusted so they show the image in a milimiter scale. If needed, an interpolation of the data between the point sensors is made afterwards, and A new run of the program with

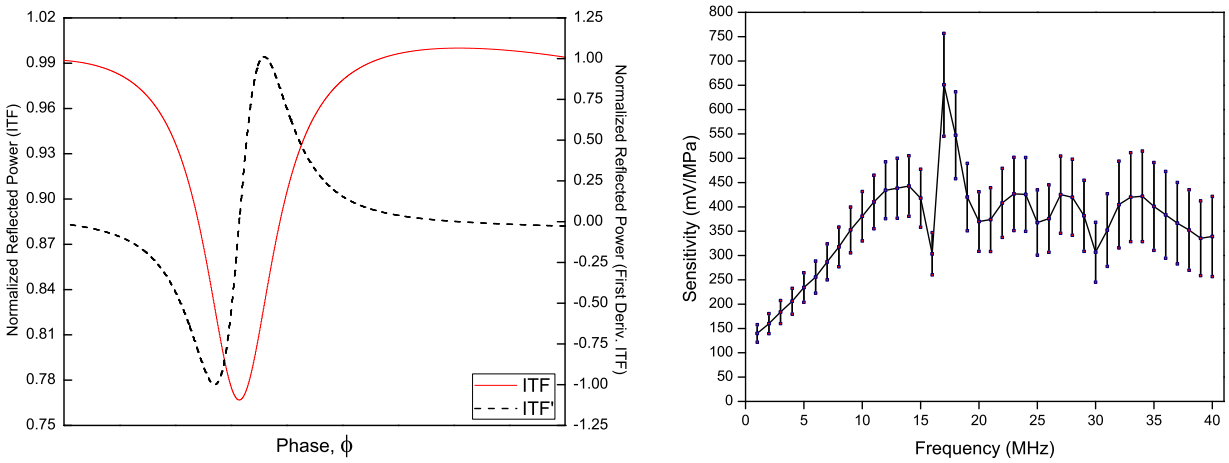

(a) Interferometer Transfer Function

(b) Sensor frequency-response sensitivity

Figure 3.10: Parameters for signal treatment.

interpolation is done to improve and visualization of edges of the imaged object.

3.5 Photoacoustic Signal Treatment

When a time signal $s_i(t)$ is detected by a linear sensor with an impulse response function $h(t)$, the output signal is given by

$$s_o(t) = s_i(t) \otimes h(t), \tag{3.1}$$

where $\otimes$ is for the convolution operation. In order to obtain a close value to the real measurement $s_i(t)$, $s_o(t)$ need to be deconvolved from $h(t)$. Then, using Fourier analysis, it can be found that the simplest way is

$$s_i(t) = \mathscr{F}^{-1}\left\{\frac{S_o(\omega)}{H(\omega)}\right\}, \tag{3.2}$$

where $\mathscr{F}^{-1}\{\}$ is the inverse Fourier transform operator, and $S_o(\omega)$, $H(\omega)$ are the Fourier transforms of $s_o(t)$ and $h(t)$, respectively.

3.6 Chapter Conclusions

The experimental setup for the measurement of thickness and for determining the experiments with phantom tissues with gold nanoparticles, is basically the same. They only differ in the excitation wavelength, and in the placing of a retarding waveplate for experiments in Section 3.3.2. The detection the acoustic wave generated along the sample remains for the circular scan in the multi-point signal detection, which leads to a photoacoustic image reconstruction. In addition, the signal treatment is possible at processing the results when the hydrophone frequency response is already has been previously obtained, like in this case.

In Chapter 4, the results corresponding to the performed experiments are shown.

Chapter 4

Results

In this chapter, the results from the experimental setups depicted in Chapter 3, are shown. The results from the measurement of thickness (or speed of sound) are shown for rubber or aluminium slabs. The experiments with phantom tissues for linearly polarized excitation light are shown afterwards. For comparison, different excitation wavelengths are used, and linear stress is applied to the tissue. For the multi-point signal detection, the circular scan allowed obtaining the measurements for a photoacoustic image reconstruction. The resulting image is compared in dimensions to the actual sample.

4.1 Measurement of Thickness

4.1.1 Rubber Slabs

In order to verify the amount of error between theoretical and experimental results, Table 4.1 shows the theoretical values for density, and speed of sound, Young modulus, and and thermal diffusivity for synthetic rubber.

Table 4.1: Synthetic Rubber Properties

Material	Density	Sp. sound	Young Mod.	Thermal Diff.
Rubber	1185 kg/m^3	1650 m/s	0.05 GPa	0.98 $\times 10^{-7}$ m^2/s

In order to ensure that the thermal and stress confinement conditions are fulfilled, calculations were made for the experiment with the rubber slab thickness. The thermal confinement is described by the following equation:

$$\tau_p \ll \frac{L_P^2}{4D_T} \tag{4.1}$$

where τ_p is the pulse time width, L_p is the characteristic linear dimension of the absorption center being heated, and D_T is the thermal diffusivity. The pulse time width is 5ns, and the linear dimension of the rubber slab was 3mm, which leads to:

$$5ns \ll \frac{(3 \times 10^{-3} m)^2}{4(0.98 \times 10^{-7} m^2/s} \longrightarrow 5ns \ll 22.95s \tag{4.2}$$

Similarly, the stress confinement condition, is described by the following equation:

$$\tau_p \ll \frac{L_p}{v} \tag{4.3}$$

where v is the speed of sound, and which leads to:

$$5ns \ll \frac{(3 \times 10^{-3} m)^2}{1650 m/s} \longrightarrow 5ns \ll 1.81\mu s \tag{4.4}$$

The acoustic signal detected by one of the transducers is in Fig. 4.1. The instants where rarefaction and compression take place in the graph are indicated. Six transducers with different characteristic sensitivities were tested for the same rubber sample. The peak-to-peak amplitude was measured for the six rarefaction signals corresponding to each hydrophone.

The average separation between the rarefaction and compression signals in the time domain, showed to be of $1.8\mu s$, which translates into a thickness of 2.97mm if a speed of sound of 1650m/s (synthetic rubber) is used.

Being the speed of sound in rubber, quite similar to the speed of sound in water, it is possible to deduce from the obtained result that a high proportion of the thickness

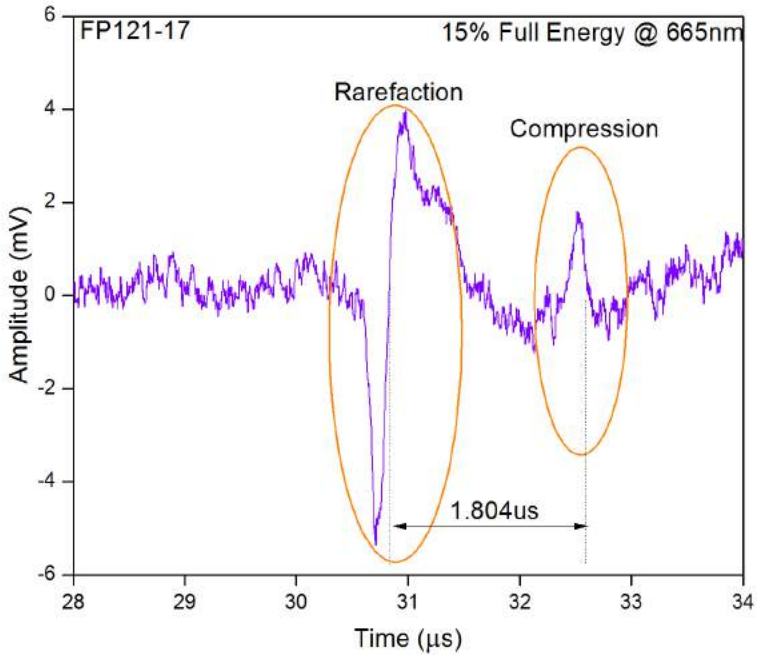

Figure 4.1: Time Domain pressure signal generated by 3mm-thick rubber slab

is being heated. The texture and flexibility of the sample allow to expect that time inversion phenomenon will be visible. In other words, the compression signal exhibits a "mirror" effect from the rarefaction signal, and indicates the difference in impedance between the first interface (water-sample) and the second (sample-water).

4.1.2 Aluminium Slabs

Same as for rubber slabs, Table 4.2 shows the theoretical values for density, and speed of sound, Young modulus and thermal diffusivity for aluminium.

Table 4.2: Aluminium Properties

Material	Density	Sp. sound	Young Mod.	Thermal Dif.
Aluminium	2.7 g/cm^3	6320 m/s	69 GPa	9.7 $\times 10^{-5}$ m^2/s

In order to ensure that the thermal and stress confinement conditions are fulfilled, calculations were made for the experiment with the rubber slab thickness. It is calculated from Eq. 4.1. The linear dimensions were 1.5mm, 3mm, 4mm and 6mm, which lead to the results on Table 4.3

Table 4.3: Thermal confinement for aluminium

Linear dimension	Thermal Confinement
1.5mm	$5ns \ll 5.79ms$
3mm	$5ns \ll 23.19ms$
4mm	$5ns \ll 41.23ms$
6mm	$5ns \ll 92.78ms$

Similarly, the stress confinement condition, is calculated from Eq. 4.3, which leads to the results on Table 4.4

Table 4.4: Stress confinement for aluminium

Linear dimension	Stress Confinement
1.5mm	$5ns \ll 0.23\mu s$
3 mm	$5ns \ll 0.47\mu s$
4 mm	$5ns \ll 0.63\mu s$
6 mm	$5ns \ll 0.95\mu s$

According to the experimental setup depicted in Fig. 3.7, the resulting photoacoustic signals produced by the four different thicknesses of the slabs, are shown in the following graphs. The results are shown both, in time domain, and in frequency domain. Due to the metallic nature of the sample, the difference in the impedance between the sample and the propagation media is larger than the difference for the previous rubber experiment. The characteristic inversion in time expected in the signal is not visible and only rarefaction signals can be seen.

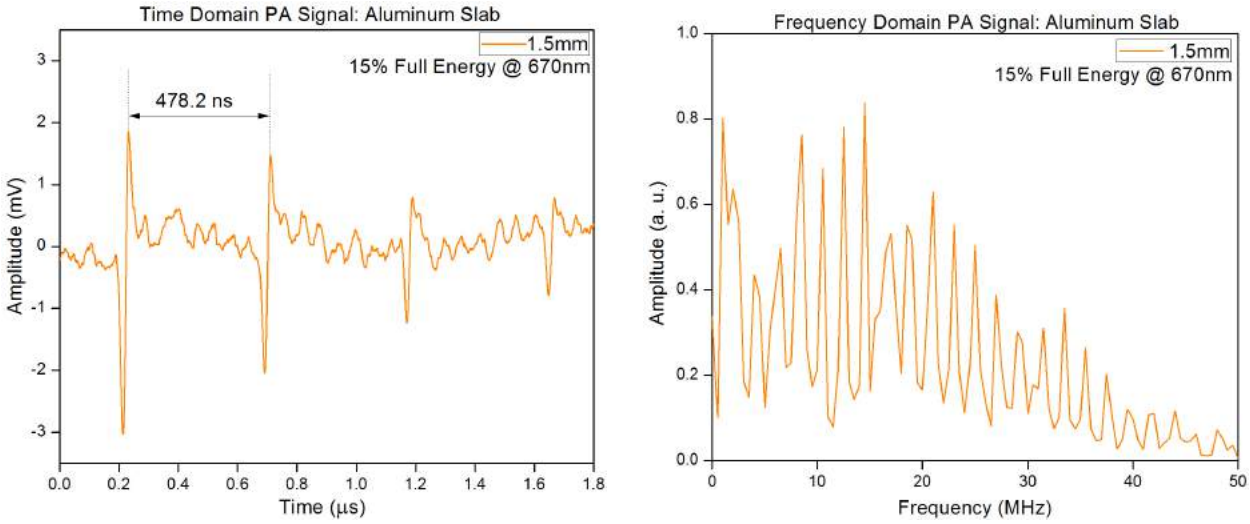

(a) Time Domain (b) Frequency Domain

Figure 4.2: Pressure signal generated by 1.5mm-thick aluminium slab

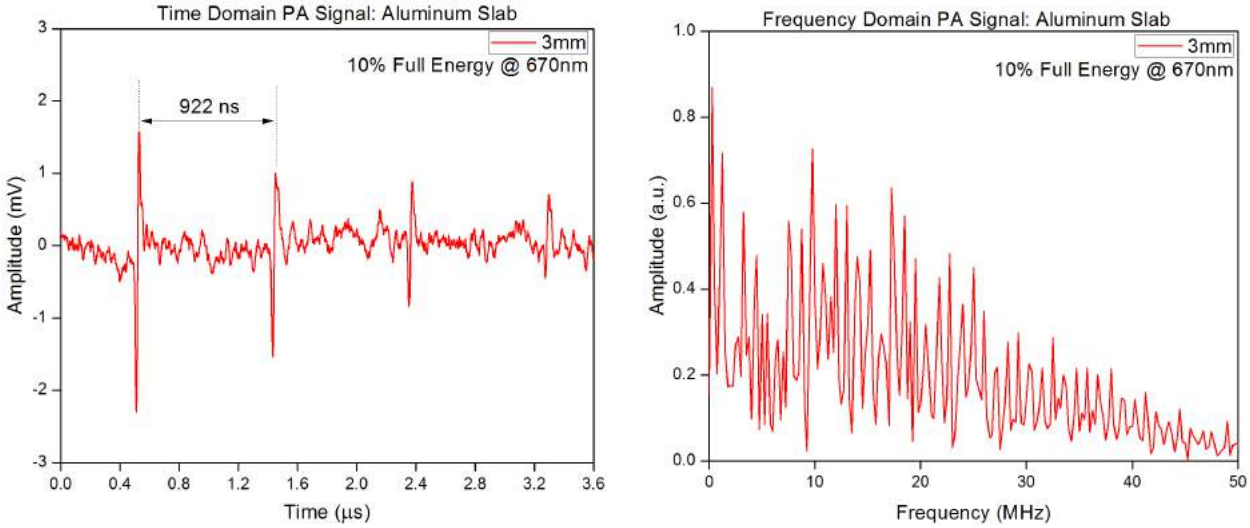

(a) Time Domain (b) Frequency Domain

Figure 4.3: Pressure signal generated by 3mm-thick aluminium slab

The time between rarefaction signals for each case is indicated. This time corresponds to the round-trip time in which the excitation energy, converted into sound, travels inside the slab. Calculations were made to find the speed of sound inside the aluminium samples and the results are depicted in Table 4.5. The average speed of sound inside the aluminum was 6341.60 m/s.

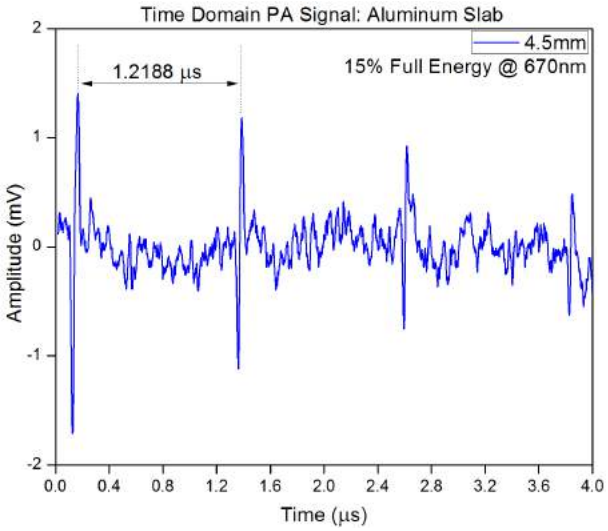

(a) Time Domain

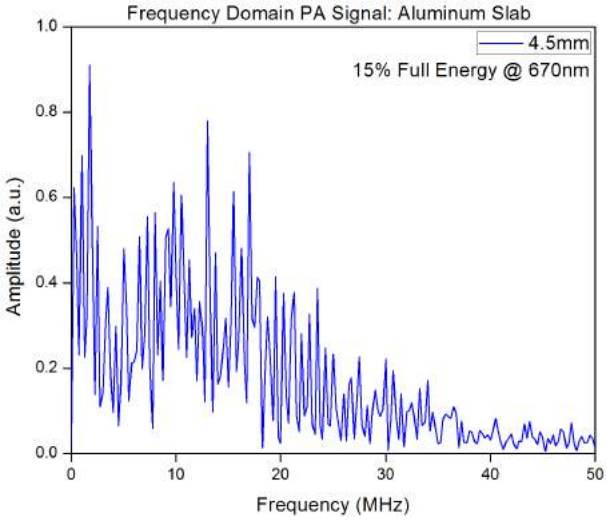

(b) Frequency Domain

Figure 4.4: Pressure signal generated by 1.5mm-thick aluminium slab

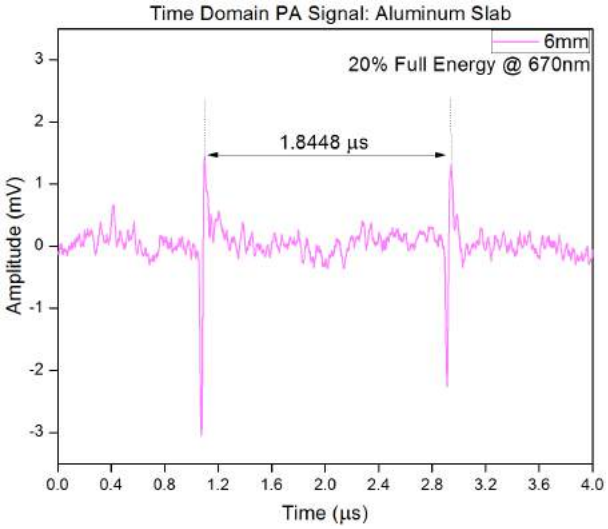

(a) Time Domain

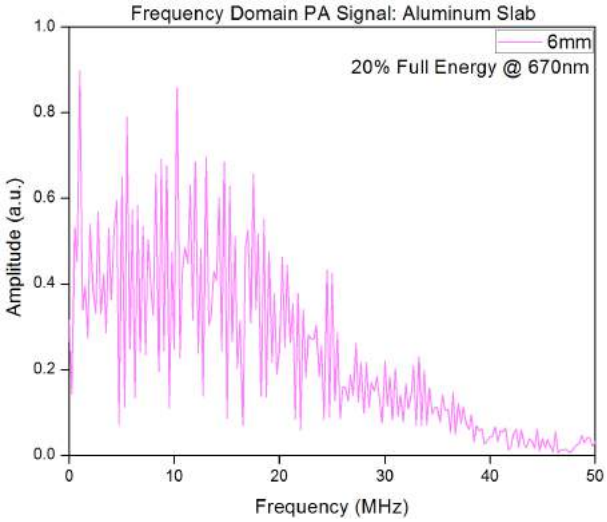

(b) Frequency Domain

Figure 4.5: Pressure signal generated by 6mm-thick aluminium slab

Table 4.5: Calculations for speed of sound in aluminium slabs

Thickness	Separation Time	Speed of sound
1.50 ± 0.006 mm	473.13 ± 9.714 ns	6340.75 ± 52.41 m/s
2.90 ± 0.006 mm	923.1 ± 0.449 ns	6283.18 ± 4.971 m/s
3.90 ± 0.006 mm	1.227 ± 0.004 μs	6356.97 ± 5.472 m/s
5.89 ± 0.006 mm	1.8448 ± 0.0002 μs	6385.51 ± 2.906 m/s

4.2 Dependence of PA signal on Light Polarization State

PASs were generated using two different excitation wavelengths: $\lambda_1 = 808$ nm and λ_2 665 nm with energy densities$E_1 = 16$ mJ/cm^2 and E2 = 17 mJ/cm^2, respectively. The latter signal has been acquired with the aim of identifying the contribution of nanoparticles to PAS. Linear polarization, in both cases, was oriented perpendicularly to the incidence plane. Thus, the electric field is parallel to the gelatin channels. Results are shown in Fig. 4.6a where each signal was averaged 128 times. It is evident that excitation using λ_1 produce ultrasound artifacts that are absent in excitation using λ_2 and they should be related to randomly distributed AuNRs. Difference between both PASs is shown in Fig. 4.6b.

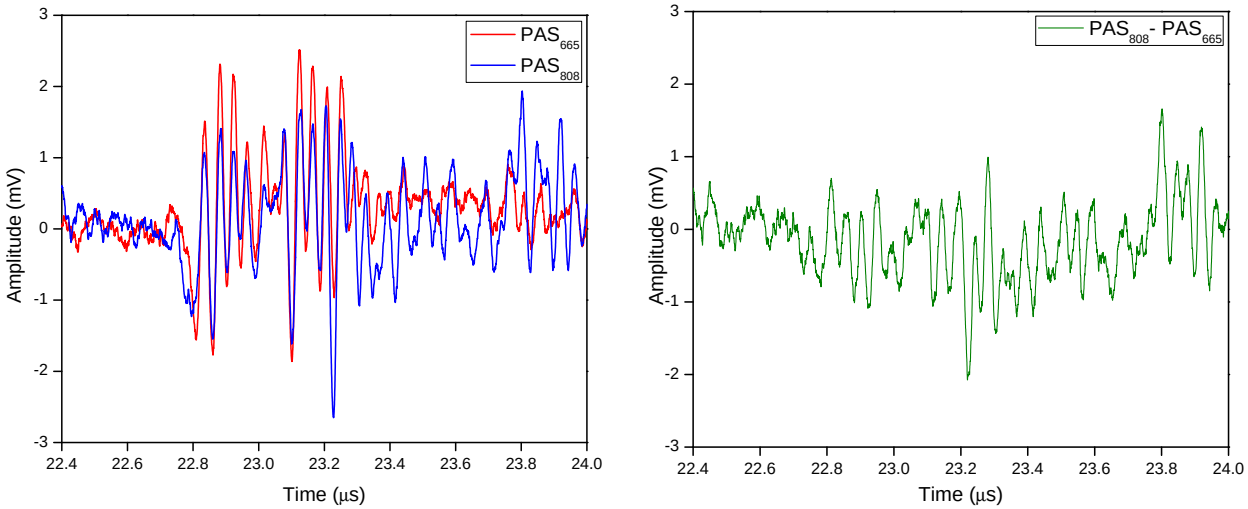

(a) Photoacoustic signals using excitation wavelengths λ_1 and λ_2.

(b) PAS difference using two different excitation wavelengths

Figure 4.6: Photoacoustic signals for AuNRs channel with two different wavelengths

Figs. 4.7a and 4.7b shows differences between PASs generated using λ_1 excitation beams with orthogonal linear polarization. In the first case, sample was evaluated 24 hours after the last freezing-thawing cycle. It was observed that there was a certain degree of AuNRs alignment along the gelatin channel. The difference amplitude increased slightly after applying an uniaxial tension along the gelatin channel. Thus, the

alignment degree of AuNRs was increased.

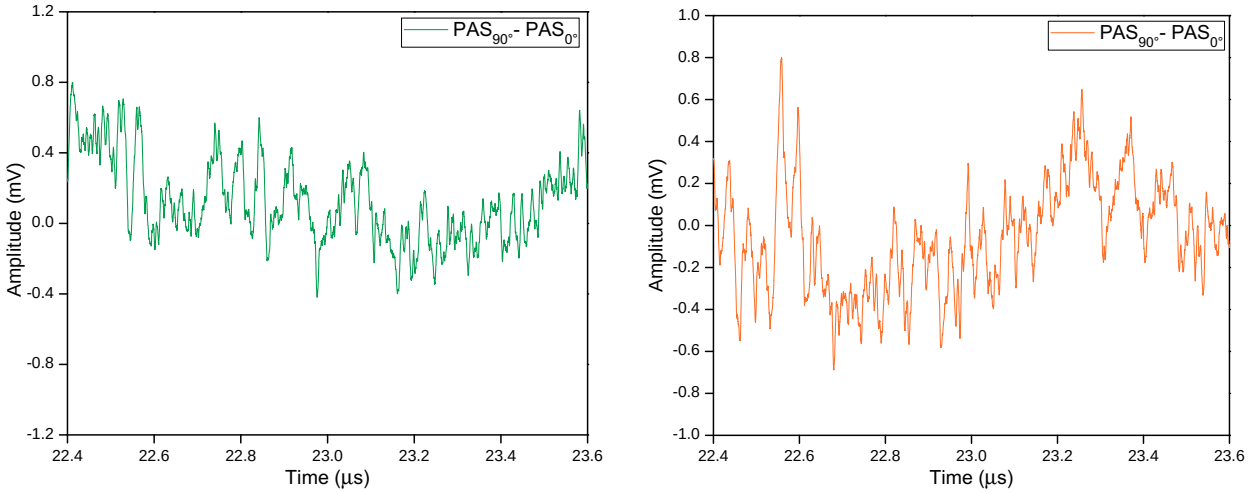

(a) Difference between PASs obtained using λ_1 excitation beams with vertical (90°) and horizontal (0°) linear polarizations

(b) Linear stress along the gelatin channel has been applied to the PVA phantom.

Figure 4.7: Photoacoustic signals for AuNRs channel (Non-stressed vs. stressed)

4.3 Multi-point signal detection for image reconstruction

Each rotation angle allows a new time-domain photoacoustic signal in transmission to be recorded. The OWIS rotary mount achieved 5-degree steps to obtain 72 measurements. On Fig. 4.8, four graphs are depicted for comparison. The graphs represent the photoacoustic signal in the time domain obtained every 90 degrees, starting at zero (reference position).

Also for the reference position at zero degrees, the photoacoustic signal obtained in frequency domain is depicted in Fig. 4.9, showing that the frequency bandwidth of the signals is around 50MHz. The remaining measurements show a very similar frequency response.

This behavior was expected by applying the Nyquist's theorem to the total frequency bandwidth of the photodetection device inside the hydrophone system. It is

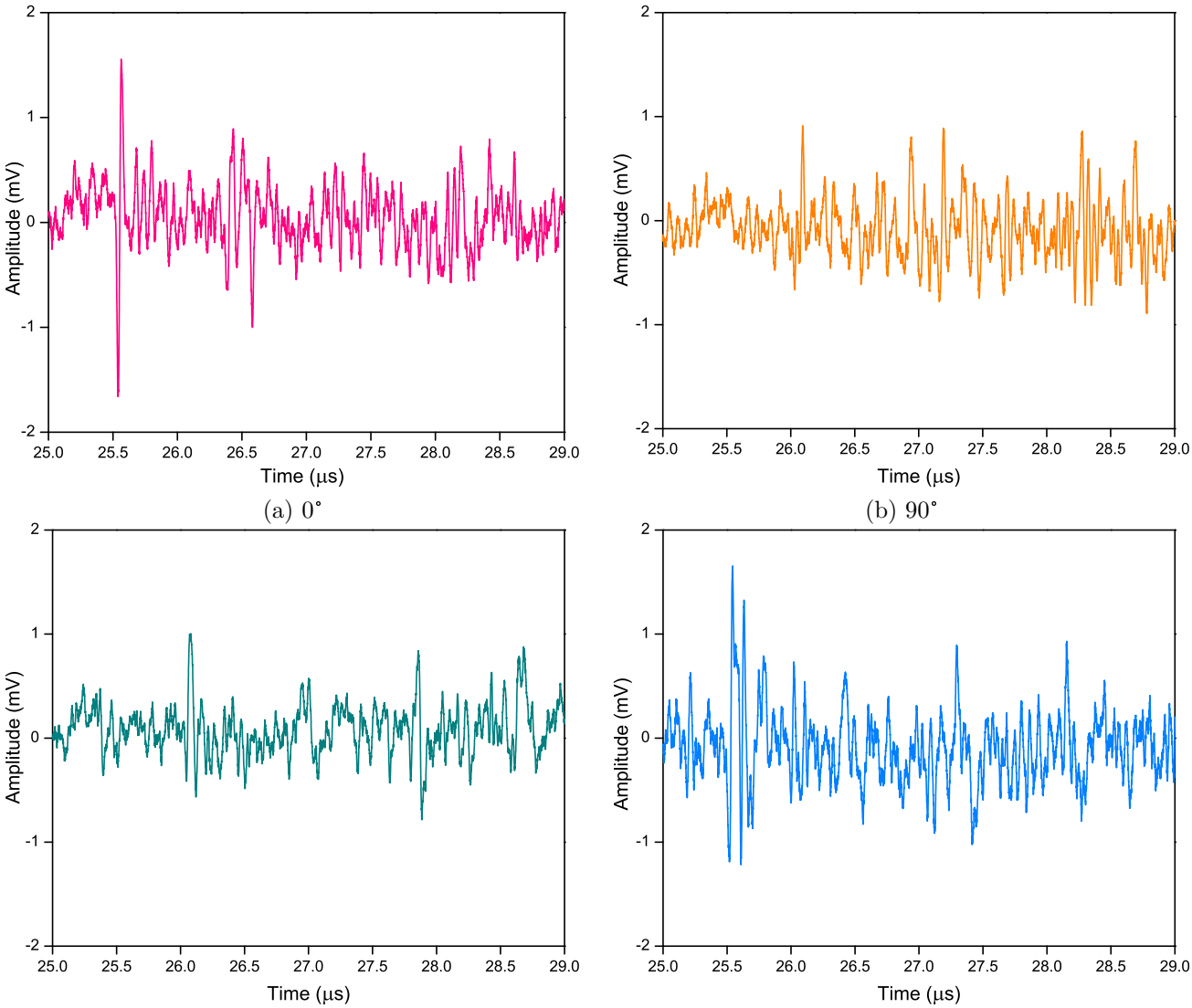

(a) 0°

(b) 90°

(c) 180°

(d) 270°

Figure 4.8: Photoacoustic Signals detected at different rotation angles

important to mention that these graphs are not filtered in frequency, and its filtering before the reconstruction of the photoacoustic image, where frequencies above 33 MHz are removed, does not produce significative reduction in the noise of the signals. Any high-frequency information of the signal beyond 30MHz is being lost in the noise.

Every frequency-domain signal acquired was individually deconvoluted from the frequency response of the sensor. Once the photoacoustic image reconstruction parameters were set, the deconvoluted pressogram matrix was introduced as the initial pressure dis-

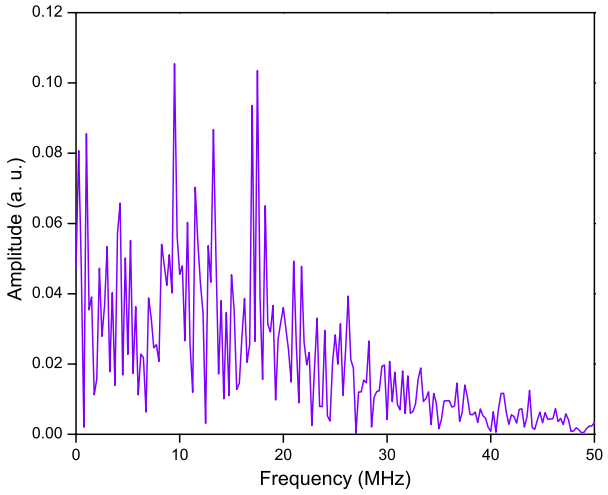

Figure 4.9: Photoacoustic signal in frequency domain for a rotation angle of 0°.

tribution. The algorithm run twice, once for each medium (water and nickel). Table 4.6 shows the theoretical values for density, and speed of sound, Young modulus and thermal diffusivity for nickel.

Table 4.6: Nickel Properties

Material	Density	Sp. sound	Young Mod.	Thermal Dif.
Aluminium	8.88 g/cm^3	6040 m/s	170 GPa	22.66 $\times 10^{-6}$ m^2/s

The average computation time was 23 minutes for the reconstruction on each case. Figure 4.10 depicts a comparison between the dimensions of the sample and the reconstructed image.

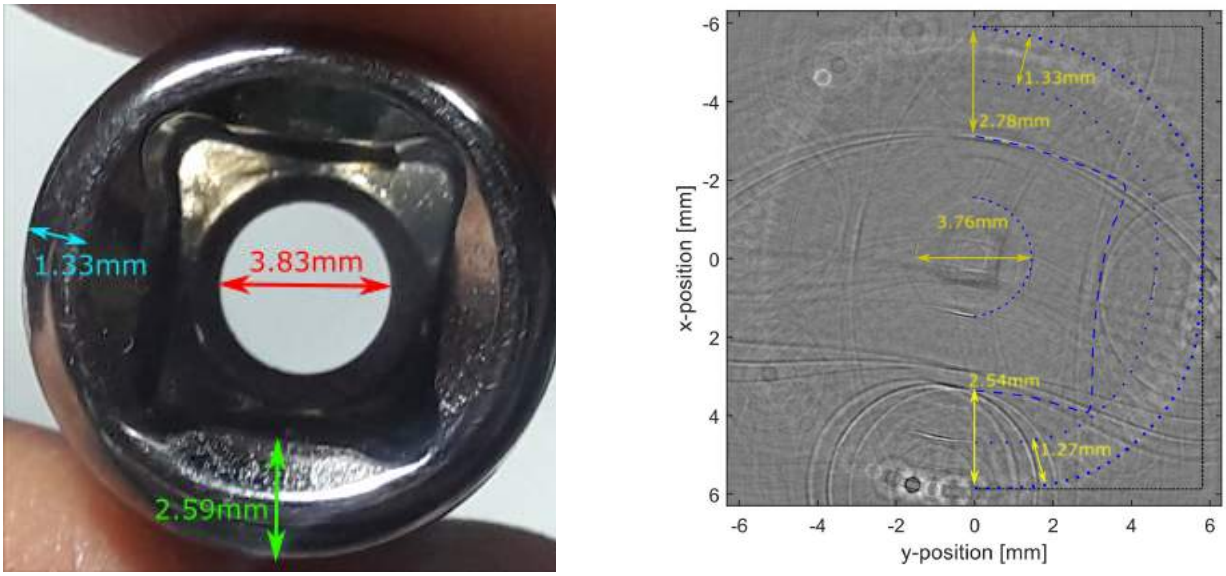

(a) Nickel sample

(b) Reconstructed Photoacoustic Image

Figure 4.10: Comparison between real and reconstructed dimensions of the sample

4.4 Discussion

The use of fiber-optic hydrophones for these experiments allowed to evaluate some photoacoustic applications. The miniaturization of sensing devices, like the case of an optical fiber with a sensing tip, increases the number of applications where these hydrophones can be used. The fact that optical fibers can bring their own advantages (high bandwidth, low noise, low weight, etc.), to any system they are part of, allows to assume that the whole system performance will be much better.

The importance of the experiments for measurement of thickness lie on the possibility to use fiber-optic sensors and photoacoustics to evaluate materials for industrial applications. In most of the literature which combine optical sensing and photoacoustics, the results reported are mainly oriented to biomedical applications, and although the extensive research in imaging attends to concerning health needs, industry could also be an opportunity to exploit the technique.

On the biomedics side, the fiber-optic hydrophones could permit the use in endo-

scopic applications, where miniaturization is one important feature for avoiding invasive imaging procedures.

The reconstructed image of a metallic sample was obtained in this thesis and there was no necessary direct contact with the sample. The dimensions of the reconstructed image where found to be very close to the actual ones. This exhibits the capability of the hydrophones to solve high-frequency spatial change (sharp edges). Reported results in [59] and [60], show the use of photoacoustics for metal detection in a phantom tissue for medical applications. However their sensing device is an ultrasound catheter limited in bandwidth by 7MHz, while the fiber-optic hydrophone used for this work was limited by 50MHz.

Imaging results with high contrast for medical imaging could be seeked by improving the sensing device and making it a sensing optical fiber.

In chapter 5, the conclusions for this thesis are presented, along with the possible future work and improvements to the experimental conditions.

Chapter 5

Conclusions and Future Work

5.1 Conclusions

The Fabry-Pérot fiber-optic hydrophones tested for the experiments of this thesis showed the expected response. From the initial hypothesis formulated, it was demonstrated that these hydrophones are suitable for photoacoustic applications. It was possible to detect pressure/acoustic signals generated by the photoacoustic effect in different samples.

The first application tested, the measurement of thickness and speed of sound in a material, thrown the same results for a number of hydrophones. Despite the fact that each hydrophone have their own frequency response, the experiment reproduced its results. The parameter to measure the thickness, was the separation time between rarefaction and/or compression signals observed in the time domain response. The separation time from the detected signal in the six transducers differed by tens of nanoseconds between each other. This allowed making an average and obtaining a very close estimation for the thickness of the material.

The frequency of the rarefaction signal (around 1 MHz for rubber, and 2.5 MHz for aluminium) was measurable for sensors where the sensitivity was higher than 120mV/MPa. Under these measurement conditions, they have certain reliability and

allow estimating, in an acceptable margin, the thickness of the synthetic rubber sample and the aluminium samples. From this, the speed of sound could also be calculated.

An interesting phenomenon occurred during the experiments. Typically, from the literature reviewed, detected pressure signals in time domain show a rarefaction signal corresponding to the first change in interface. The second change in interface corresponds to the compression signal, which is often inverted in time domain. This phenomenon could be observed only for the rubber sample, not for aluminium. The latter throws the conclusion that materials with a similar speed of sound to the propagation medium will have the expected behavior explained by the photoacoustics rigorous theory. For the case of materials with a much larger speed of sound, the thickness can be determined by the time period at which rarefaction signals (correspondent to the internal reflections) appear.

For the second application tested, the dependence of the photoacoustic signal (PAS) on polarization state, the difference in PASs obtained with orthogonal linear polarizations in the excitation light beam showed that gold nanorods (AuNRs) were aligned to a small degree along the gelatin channels. This ordering during the last freezing-thawing cycle applied to the cryogel was incremented after applying a tensile strain along the gelatin channel containing the AuNRs. The detection of photoacoustic signals with the use of Fabry-Pérot interferometric hydrophones for this application was also demonstrated. There was a visible change in amplitude of the PAS when the gelatin channel had applied stress, and also, a visible change in the shape of the signal when the sample is illuminated with different polarization states of light. Anisotropic materials like the AuNRs, are then, dependent on the polarization state of light.

For the third and final application, the possibility for image reconstruction, the experiment was carried out by detecting the transmitted signal through the sample. The signals could be recovered and the amplitude was high enough as to perform a reconstruction, thanks to the high sensitivity of the hydrophone used in this work. It was possible to recover smaller features of the sample, such as the semi-squared inner shape, and an inner smaller circular shape.

The approach to the inverse photoacoustic problem solved by the k-Wave toolbox functions result in an admissible first approximation. The results indicate that the signals were correctly acquired for a metallic sample. However, the experiment can be improved. The extended bandwidth offered by fiber-optic systems is being limited by the photodetection device inside the hydrophone system (100 MHz). A noise filtering stage introduced before the pre-amplification circuit could be added to the photodetection system to reduce the joint noise introduced by the photodetector itself and the BNC connectors between the system and the oscilloscope.

Summarizing, these last results appear promising and highlight the areas of opportunity for further research where this experiment can be improved. A low-noise photodetection device with higher bandwidth is required if small details of samples are to be detected. Among the open problems of photoacoustic imaging, the inverse photoacoustic problem approach could still be improved and adjusted to particular applications, detection geometries, and specific experiment parameters. Finally, further experiments could test the proposed setup by increasing the number of transducers, the array geometry or by using different metallic samples.

5.2 Future Work

The interpretation of the thickness measurement results may suggest the possible measurement of thickness for other materials which produce an acoustic signal when radiated with a certain wavelength. This opens the possibility of using the technique for industrial applications. For biomedical applications, when optically anisotropic biomarkers are introduced in structured tissue it can provide additional information.

On the sensing system, a low-noise photodetection device with higher bandwidth is required if small details of samples want to be detected. Improving the sensing system will result in detected pressure signals with higher quality. The ability of optical sensors to detect pressure signals can be exploited for biomedical imaging if better signals are detected, along with the small size provided by optical fibers, in particular.

Between the open problems of photoacoustic imaging, the inverse photoacoustic problem approach still has to be improved and more complex to be adjusted to particular applications. Variables such as the temporal profile of the laser pulse, and more complicated geometries could be introduced to the ohotoacoustics wave equations, in order to observe and compare expected versus obtained results. That is one of the features which represent the next step towards quantitative photoacoustic tomography.

The MATLAB k-Wave toolbox is an excellent open-source tool for image reconstruction. The functions and example algorithm codes can still be modified to be adjusted to specific experiments. In addition, new algorithms can be developed in the future, inspired on the k-Wave functions in different programming languages.

Bibliography

[1] A. I. Ltd., "Piezoelectric constants," 2012.

[2] S. Manohar and D. Razansky, "Photoacoustics: a historical review," *Advances in Optics and Photonics*, vol. 8, no. 4, pp. 586–617, 2016.

[3] L. Amar, M. Bruma, P. Desvignes, M. Leblanc, G. Perdriel, and M. Velghe, "Detection, on the occipital bone, of elastic (ultrasonic) waves induced by laser impulses in the eye of a rabbit," *Comptes rendus hebdomadaires des séances de l'Académie des sciences*, vol. 259, pp. 3653–3655, 1964.

[4] N. R. Council *et al.*, *Expanding the vision of sensor materials*. National Academies Press, 1995.

[5] H. Kuttruff, *Acoustics: an introduction*. CRC Press, 2007.

[6] M. Martinez, *Investigación y Desarrollo de un Sensor de Fibra Optica Distribuido para la Detección de Vibraciones*. PhD thesis, Tesis de maestrıa, CICESE, 2008.

[7] N. R. Center, "Ultrasonic testing," 2014.

[8] S. Srinivasan, B. W. Pogue, S. Jiang, H. Dehghani, C. Kogel, S. Soho, J. J. Gibson, T. D. Tosteson, S. P. Poplack, and K. D. Paulsen, "Interpreting hemoglobin and water concentration, oxygen saturation, and scattering measured in vivo by near-infrared breast tomography," *Proceedings of the National Academy of Sciences*, vol. 100, no. 21, pp. 12349–12354, 2003.

[9] A. E. Cerussi, A. J. Berger, F. Bevilacqua, N. Shah, D. Jakubowski, J. Butler, R. F. Holcombe, and B. J. Tromberg, "Sources of absorption and scattering contrast for near-infrared optical mammography," *Academic radiology*, vol. 8, no. 3, pp. 211–218, 2001.

[10] N. R. Center, "Radiographic testing," 2014.

[11] W. Smith, "The action of light on selenium," *Journal of the Society of Telegraph Engineers*, vol. 2, no. 4, pp. 31–33, 1873.

[12] A. G. Bell, "On the production and reproduction of sound by light," *American Journal of Science*, no. 118, pp. 305–324, 1880.

[13] A. G. Bell, "Selenium and the photophone," *Nature*, vol. 22, no. 569, pp. 500–503, 1880.

[14] A. G. Bell, "Production of sound by radiant energy," *J. Franklin Inst.*, 1881.

[15] A. Bell, "The spectrophone," *Bull. Phil. Soc*, vol. 4, pp. 143–162, 1881.

[16] M. Viengerov, "New method of gas analysis based on tyndall-roentgen optoacoustic effect," *Doklady Akademii Nauk SSSR*, vol. 19, no. 687, p. 8, 1938.

[17] A. Pfund, "Atmospheric contamination," *Science*, vol. 90, no. 2336, pp. 326–327, 1939.

[18] K. Luft, "Infrared techniques for the measurement of carbon monoxide," *Annals of Occupational Hygiene*, vol. 18, no. 1, pp. 45–51, 1975.

[19] K. Luft, "Über eine neue methode der registrierenden gasanalyse mit hilfe der absorption ultraroter strahlen ohne spektrale zerlegung," *Z. tech. Phys*, vol. 24, pp. 97–104, 1943.

[20] A. Mandelis, "Diffusion waves and their uses," *Physics today*, vol. 53, no. 8, pp. 29–34, 2000.

[21] A. Ångstrom, "Neue methode, das wärmeleitungsvermögen der körper zu bestimmen," *Annalen der Physik*, vol. 190, no. 12, pp. 513–530, 1862.

[22] W. H. Preece, "On the conversion of radiant energy into sonorous vibrations," *Proceedings of the Royal Society of London*, vol. 31, no. 206-211, pp. 506–520, 1880.

[23] M. E. Mercadier, "J'appelle radiophonie le phénomène nouveau auquel m. g. bell," 1881.

[24] M. E. Mercadier, "Pondre aux diverses questions que soulève lapratique, qu'il s' agisse," 1881.

[25] L. Rayleigh, "The photophone," *Nature*, vol. 23, no. 586, pp. 274–275, 1881.

[26] A. Rosencwaig and A. Gersho, "Photoacoustic effect with solids: a theoretical treatment," *Science*, vol. 190, pp. 556–557, 1975.

[27] A. Rosencwaig and A. Gersho, "Theory of the photoacoustic effect with solids," *Journal of Applied Physics*, vol. 47, no. 1, pp. 64–69, 1976.

[28] A. Boccara, D. Fournier, and J. Badoz, "Thermo-optical spectroscopy: Detection by the"mirage effect"," *Applied Physics Letters*, vol. 36, no. 2, pp. 130–132, 1980.

[29] A. Mandelis, "Frequency-domain photopyroelectric spectroscopy of condensed phases (ppes): A new, simple and powerful spectroscopic technique," *Chemical physics letters*, vol. 108, no. 4, pp. 388–392, 1984.

[30] P.-E. Nordal and S. O. Kanstad, "Photothermal radiometry," *Physica Scripta*, vol. 20, no. 5-6, p. 659, 1979.

[31] E. L. Kerr and J. G. Atwood, "The laser illuminated absorptivity spectrophone: a method for measurement of weak absorptivity in gases at laser wavelengths," *Applied optics*, vol. 7, no. 5, pp. 915–921, 1968.

[32] F. A. Duck, *Physical properties of tissues: a comprehensive reference book*. Academic press, 2013.

[33] H. S. Carslaw and J. C. Jaeger, "Conduction of heat in solids," *Oxford: Clarendon Press, 1959, 2nd ed.*, 1959.

[34] L. Wang and H.-i. Wu, "Biomedical optics: Principles and imaging wiley," *New York*, 2007.

[35] S. L. Jacques, "Role of tissue optics and pulse duration on tissue effects during high-power laser irradiation," *Applied Optics*, vol. 32, no. 13, pp. 2447–2454, 1993.

[36] A. Karabutov, N. Podymova, and V. Letokhov, "Time-resolved laser optoacoustic tomography of inhomogeneous media," *Applied Physics B*, vol. 63, no. 6, pp. 545–563, 1996.

[37] *Laser Optoacoustics*. American Institute of Physics, 1993.

[38] A. Rosencwaig, "Photoacoustic spectroscopy of solids," *Optics Communications*, vol. 7, no. 4, pp. 305–308, 1973.

[39] W. R. Harshbarger and M. B. Robin, "Opto-acoustic effect. revival of an old technique for molecular spectroscopy," *Accounts of chemical research*, vol. 6, no. 10, pp. 329–334, 1973.

[40] A. Rosencwaig, *Photoacoustics and photoacoustic spectroscopy*. Wiley, 1980.

[41] L. Amar, M. Bruma, M. Velghe, and P. Desvignes, "On the detection of laser induced ultrasonic waves in the human eye and the elaboration of a theory on the fundamental mechanism of vision," *Zeitschrift für angewandte Mathematik und Physik ZAMP*, vol. 16, no. 1, pp. 182–183, 1965.

[42] S. F. Cleary and P. E. Hamrick, "Laser-induced acoustic transients in the mammalian eye," *The Journal of the Acoustical Society of America*, vol. 46, no. 4B, pp. 1037–1044, 1969.

[43] A. H. Frey *et al.*, "Auditory system response to radiofrequency energy," *Aerospace med*, vol. 32, no. 1, pp. 1140–1142, 1961.

[44] A. H. Frey and R. Messenger, "Human perception of illumination with pulsed ultrahigh-frequency electromagnetic energy," *Science*, vol. 181, no. 4097, pp. 356–358, 1973.

[45] J. Sharp, H. Grove, and O. Gandhi, "Generation of acoustic signals by pulsed microwave energy (letters)," *IEEE Transactions on Microwave Theory and Techniques*, vol. 22, no. 5, pp. 583–584, 1974.

[46] J. Elder and C. Chou, "Auditory response to pulsed radiofrequency energy," *Bioelectromagnetics*, vol. 24, no. S6, 2003.

[47] K. R. Foster and E. D. Finch, "Microwave hearing: evidence for thermoacoustic auditory stimulation by pulsed microwaves," *Science*, vol. 185, no. 4147, pp. 256–258, 1974.

[48] D. Borth and C. Cain, "Theoretical analysis of acoustic signal generation in materials irradiated with microwave energy," *IEEE Transactions on Microwave Theory and Techniques*, vol. 25, no. 11, pp. 944–954, 1977.

[49] A. Rosencwaig, "Photoacoustic spectroscopy," *Advances in electronics and electron physics*, vol. 46, pp. 207–311, 1978.

[50] S. D. Campbell, S. S. Yee, and M. A. Afromowitz, "Applications of photoacoustic spectroscopy to problems in dermatology research," *IEEE Transactions on Biomedical Engineering*, no. 4, pp. 220–227, 1979.

[51] R. G. Olsen and W. C. Hammer, "Microwave-induced pressure waves in a model of muscle tissue," *Bioelectromagnetics*, vol. 1, no. 1, pp. 45–54, 1980.

[52] T. Bowen, "Radiation-induced thermoacoustic soft tissue imaging," in *Ultrasonics Symposium*.

[53] T. Bowen, R. Nasoni, A. Pifer, and G. Sembroski, "Some experimental results on the thermoacoustic imaging of tissue equivalent phantom materials," in *1981 Ultrasonics Symposium*, pp. 823–827, IEEE, 1981.

[54] P. Morris, A. Hurrell, A. Shaw, E. Zhang, and P. Beard, "A fabry–pérot fiber-optic ultrasonic hydrophone for the simultaneous measurement of temperature and acoustic pressure," *J. of the Acoustical Soc. of America*, vol. 125, no. 6, pp. 3611–3622, 2009.

[55] L. V. Wang, *Photoacoustic imaging and spectroscopy*. CRC press, 2009.

[56] H. Jiang, *Photoacoustic Tomography*. CRC Press Boca Raton, FL, 2015.

[57] O. Scherzer, *Handbook of mathematical methods in imaging*. Springer Science & Business Media, 2015.

[58] B. E. Treeby and B. T. Cox, "k-wave: Matlab toolbox for the simulation and reconstruction of photoacoustic wave fields," *J. of Biomedical Optics*, vol. 15, no. 2, pp. 021314–021314, 2010.

[59] J. L. Su, B. Wang, and S. Y. Emelianov, "Photoacoustic imaging of coronary artery stents," *Opt. Express*, vol. 17, no. 22, pp. 19894–19901, 2009.

[60] J. Su, A. Karpiouk, B. Wang, and S. Emelianov, "Photoacoustic imaging of clinical metal needles in tissue," *J. Biomed. Opt.*, vol. 15, no. 2, pp. 021309–021309, 2010.